CHALMERS
UNIVERSITY OF TECHNOLOGY

Thermal Simulation of Vehicle Under-hood Region

Methodology for Conjugate Heat Transfer simulation of a full-scale truck using STAR-CCM+

Degree project report in Applied Mechanics

Joseph Tyler Angelico
Omkar Nagrenda Kashyap

DEPARTMENT OF MECHANICS AND MARITIME SCIENCES

CHALMERS UNIVERSITY OF TECHNOLOGY
Gothenburg, Sweden 2024
www.chalmers.se

Degree project report 2024

Thermal Simulation of Vehicle Under-hood Region

Methodology development of Conjugate Heat Transfer of full-scale truck coupled with thermal flow simulation in STAR-CCM+

Joseph Tyler Angelico
Omkar Nagrenda Kashyap

CHALMERS
UNIVERSITY OF TECHNOLOGY

Department of Mechanics and Maritime Sciences
Chalmers University of Technology
Gothenburg, Sweden 2024

Methodology development of Conjugate Heat Transfer of full-scale truck coupled with under-hood thermal flow simulation in STARCCM+
JOSEPH TYLER ANGELICO
OMKAR NAGENDRA KASHYAP

Supervisor: Sudharsan Vasudevan, Volvo Trucks
Examiner: Sassan Etemad, Mechanics & Maritime Sciences

Degree project report 2024
Department of Mechanics & Maritime Sciences
Chalmers University of Technology
SE-412 96 Gothenburg
Sweden
Telephone +46 31 772 1000

Cover: Front view of an FH truck model colored wall $y+$ values

Typeset in LaTeX
Gothenburg, Sweden 2024

Thermal Simulation of Vehicle Under-hood
Methodology for Conjugate Heat Transfer simulation of a full-scale truck using STAR-CCM+
JOSEPH TYLER ANGELICO
OMKAR NAGENDRA KASHYAP
Department of Mechanics & Maritime Sciences
Chalmers University of Technology

Abstract

Trucks with internal combustion engines (ICE) represent a significant majority of the EU long haul freight sector due to their reliability, refueling infrastructure, and versatility in handling highly varied environmental conditions. As noise and emission regulations continue to become more stringent, the current and future fleets of ICE vehicles continue to face highly technical challenges in maintaining thermal performance while meeting new standards. As a result the need for an efficient simulation methodology has never been more critical for driving timely design evolution. Today, these simulations are typically performed through co-simulations with multiple software packages to resolve radiation and convection heat transfer phenomena. This study looks to develop a streamlined conjugate heat transfer simulation methodology within Siemens STAR-CCM+ Computational Fluid Dynamics (CFD) software. A Volvo truck model was simulated utilizing a simplified under-hood. The simulation was compared against limited experimental data for four different steady-state engine operating conditions. The results from the simulations corroborated well with the test data for the chosen components. Further development of such a method will lead to a viable solution for full-scale under-hood simulations using only STAR-CCM+, i.e., within a single simulation model.

Keywords: Under-hood, Conjugate Heat Transfer, conduction, convection, radiation

Acknowledgements

We would like to thank Volvo Group Trucks Technologies for sponsoring the thesis work, and Chalmers University of Technology for facilitating the opportunity. We would like to thank Sudharsan Vasudevan, our supervisor, Torbjörn Wiklund, our co-supervisor for their guidance throughout the project, and Sassam Etemad, our Examiner, for his support. We'd like to acknowledge the whole Thermal Management team at VGTT, particularly Zenitha Chroneér and Bruno Bartolec for their support with STAR-CCM+, as well as Jérôme Rosenwald for opening the positions. Additionally, we'd like to recognize Alexandre Cano for his time and insights on various aspects of STAR-CCM+ CHT not explored in this thesis work.

We would like to acknowledge BETA-CAE for providing academic licenses for ANSA pre-processor and Siemens for providing academic licenses for STAR-CCM+ for use in the thesis.

Lastly, we'd like to thank our friends and family for supporting us through the whole process.

Joseph Angelico &
Omkar Kashyap, Gothenburg, July 2024

List of Acronyms

Below is the list of acronyms that have been used throughout this thesis listed in alphabetical order:

ACEA	l'Association des Constructeurs Européens d'Automobiles (European Automobile Manufacturers' Association)
AVU	Air Value Unit
CAC	Charge Air Cooler
CLB	Close-loop Butterfy Value
ECU	Electronic Control Unit
EGR	Exhaust Gas Recirculator
EU	European Union
CFD	Computational Fluid Dynamics
CHT	Conjugate Heat Transfer
FEM	Finite Element Method
FFH	Fuel Filter Housing
FPF	Fuel Particulate Filters
FVM	Finite Volume Method
HTC	Heat Transfer Coefficient
LES	Large Eddy Simulation
LHS	Left-hand side (relative to driver)
RANS	Reynolds-Averaged Navier-Stokes
RHS	Right-hand side (relative to driver)
RKE	Realizable k-ϵ
RKE 2L	Realizable k-ϵ Two-Layer
SFE	Segregated Fluid Enthalpy
SFI	Segregated Fluid Isothermal
SFT	Segregated Fluid Temperature
SKE	Standard k-ϵ
SKE 2L	Standard k-ϵ Two-Layer
SKO	Standard k-ω
SSTKO	Shear Stress Transport K-ω
TC	Turbo Compound

Nomenclature

Below is the nomenclature of indices, sets, parameters, and variables that have been used throughout this thesis.

Variables

ϕ	Transport Variable
S_u	Source Term
ρ	Density
t	Time
dX	Differential of X
$\mathbf{v}$	Velocity
p	Pressure
f_b	Body Force
$\mathbf{D}$	Rate of Deformation Tensor
E	Energy
R	Specific Gas Constant
R_u	Universal Gas Constant
$\overline{X}$	Average of X
$\mathbf{q}$	Heat Flux
k	Thermal Conductivity
T	Temperature
ΔX	Change in X
h	Convective Heat Transfer Coefficient
Re	Reynolds Number
L	Characteristic Length
μ	Absolute Viscosity
c_p	Specific Heat

ν	Molecular Diffusivity
α	Thermal Diffusivity
Pr	Prandtl Number
Gr	Grashof Number
Ra	Rayleigh Number
β	Coefficient of Volume Expansion
Nu	Nusselt Number
σ_{ij}	Stefan-Boltzmann Constant
$\boldsymbol{\sigma}$	Stress tensor
ϵ	Emissivity
ω	Rotation Speed
ψ	Volume Flow Rate
$\dot{m}$	Mass Flow Rate
$Q_{convective}$	Magnitude of Convective Heat Transfer
$T_{ambient}$	Temperature of Ambient
T_{max}	Maximum temperature
T_{avg}	Average temperature

Contents

List of Figures

List of Tables

1
Introduction

1.1 Background and Motivation

The truck industry has been the backbone of transportation of freight in Europe. Over 77% of all freight transported across the European Union is through trucks, of which 99.9% on the road today utilize an Internal Combustion Engine (ICE) [1]. ICE trucks dominate the long haul freight sector due to their reliability, the refueling infrastructure, the ability to carry heavy loads over long distances, and their versatility in handling extreme weather conditions. With the advancements in the development of alternate ICE fuels and hybrid drive-trains, ICE trucks will continue to be a significant part of the long haul freight fleet for the foreseeable future.
As sustainability standards and regulations continue to progress, ICE vehicle designs will also need to evolve in lock step. Modern emission and noise regulations such as Council of the EU's Euro 7 [2] and emission proposals [3], as well as modern Environmental Noise Directives [4] require design solutions that tend to impact thermal management. These regulations when coupled with an ever increasing competitive need for design changes to increase fuel efficiency, often at the potential compromise of thermal management [5], have lead to unprecedented thermal design challenges. It has become increasingly critical that designs are validated as early as possible to identify any potential thermal failure and subsequent design iterations before physical testing. This motivates the need for robust yet relatively computational and efficient simulations of the under-hood thermal environment.

In a standard European truck design, the section of the truck underneath the cabin that houses the engine and other key components of the vehicle is referred to as the under-hood region. This region is highly complex as it not only houses the powertrain of the vehicle, but also necessary auxiliary systems that enable effective operation of the powertrain such as coolant systems, intake and exhaust systems, electronic control units (ECU), fuel and oil filters and pumps, etc. The vehicle under-hood region is shown in Figure 1.1 below.

Given the importance, development of under-hood thermal simulation models have been ongoing for over two decades. Common industrial practice, however, typically involves the use of co-simulations. These co-simulations may include two distinct simulations coupled from the same software as was performed in [6], or more commonly, coupling independant radiation and conduction solving software (such as RADTherm, PowerTHERM, etc.) with flow solving software (STAR-CCM+, Pow-

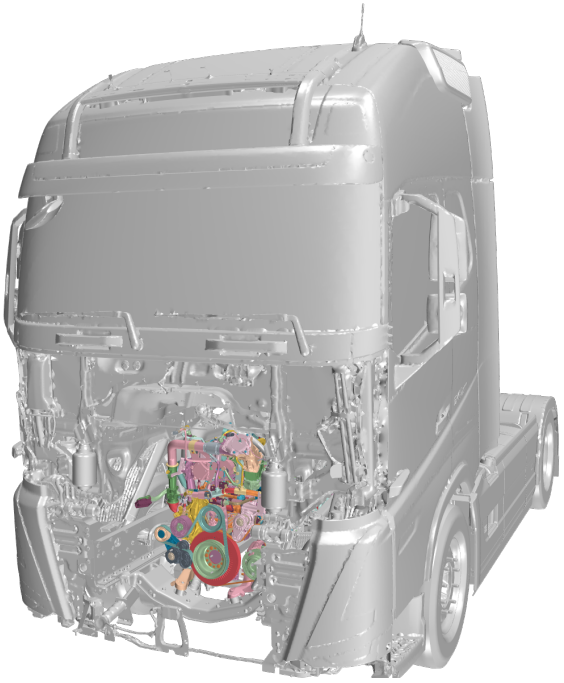

Figure 1.1: Vehicle Under-hood in color, grille and coolant system not included

erFLOW, FLUENT, etc.) as seen in [7], [8] and [9].

The need to utilize multiple sets of software creates a cumbersome initialization process. The goal of this work is the development of a streamlined process that aims at reducing the resource cost of simulation initialization, freeing resources to perform simulations at different conditions more accessibly. Currently, this will be explored through attempting thermal modeling completely in a single simulation within STAR-CCM+.

1.2 Objective

The main objective of this project is to develop a CHT simulation methodology, which comprises of the following:

- Develop a model that is capable of solving under-hood flow simulations and Conjugate Heat Transfer simulations in a single model on a single platform using a single file.
- Perform parametric studies of the simulation parameters given below to understand their influence on the simulation results:
  - CHT continua communication
  - Looping frequency
  - Turbulence model
  - Type of mesh
  - Radiation patch-face proportion

1.3 Vehicle Model

The vehicle model provided by Volvo is a Euro FH truck with a 13L 540hP diesel engine. The engine configuration consisted of a turbocharged 6-cylinder diesel engine equipped with a charge air cooler (CAC), exhaust gas recirculation (EGR) and turbo-compound (TC) unit. The CAC, also known as an intercooler, works to cool the compressed air from the compressor of the turbocharger, increasing the air density and subsequently combustion efficiency. The EGR system works to decrease harmful exhaust emissions, particularly NOx, by recirculating the cooled engine exhaust back into the engine intake, decreasing the amount of oxygen and thus lowering the resulting combustion temperature. This temperature reduction lowers the amount of NOx that is created during the combustion process [10]. The TC also increases fuel efficiency by harnessing the remaining energy in the exhaust gas after the turbocharger to directly feed power into the engine flywheel via an additional turbine.

The CAC is typically located within the cooling system at the front of the vehicle, behind the grille. The primary components of the cooling system are shown in the simplified schematic in Figure 1.2 below. Together, these components can be referred to as the cooling pack, which is made up of the condenser, the charged air cooler, and the main radiator. The engine fan is then enshrouded immediately behind the radiator, pulling the air through the cooling pack and into the under-hood. The connecting lines in Figure 1.2 indicate air ducting and flow.

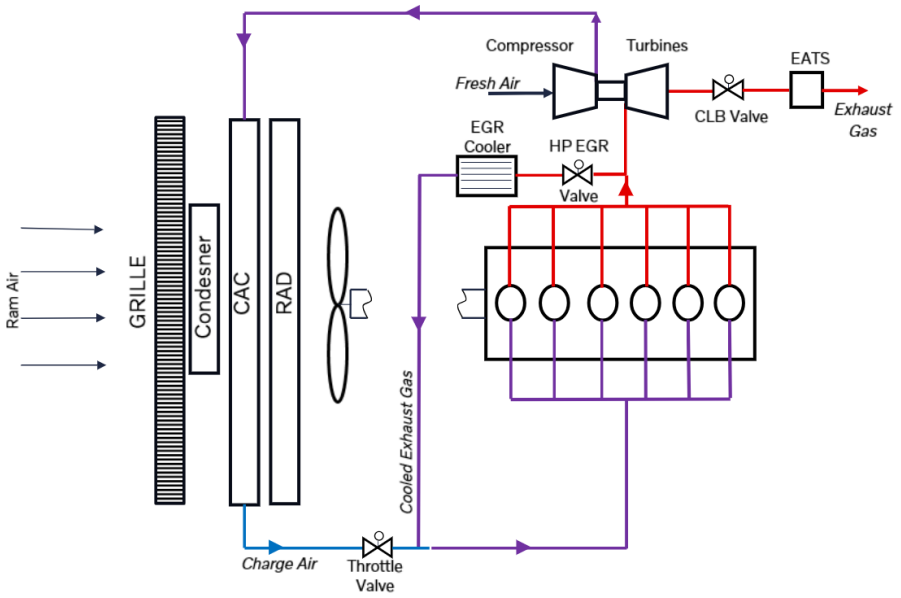

Figure 1.2: Simplified schematic of the under-hood. Coolant Loop not shown

1.4 The Under-hood Thermal Environment

Each of the aforementioned additional components and systems have an effect on the thermal environment. The CAC, for instance, effectively increases the cooling air temperature entering the under-hood as the energy is transferred from the charged engine intake air to the ram air, which, in turn, flows into the under-hood region. The EGR's impact, while much more complex, also increases the bulk air temperature entering the under-hood through transferring the thermal energy from the hot exhaust gas to coolant, which then transfers a portion of this additional energy back into the cooling air entering the under-hood. The EGR system, primarily through the EGR valve and cooler, also acts as additional radiative heat sources on the right side of the under-hood.

The left and right hand side of the under-hood are generally dominated by differing modes of heat transfer. The Right Hand Side (RHS) is dominated by radiative heat transfer. This is because the major heat sources within the under-hood are located on this side. These heat sources are primarily composed of components handling exhaust gas, such as the exhaust manifold, the turbo-compound, the closed-loop butterfly value, exhaust pipe, and the EGR components. Left Hand Side (LHS) is convection-dominant, as without major heat sources located on this side, forced convection drives the heat transfer in this area. The airflow into the under-hood is dictated by vehicle speed and fan speed when the engine is running. The air temperature is highly dependent on ambient driving conditions as well as the heat rejected from the cooling pack radiator. Figure 1.3 below defines these two regions from a top view of the truck.

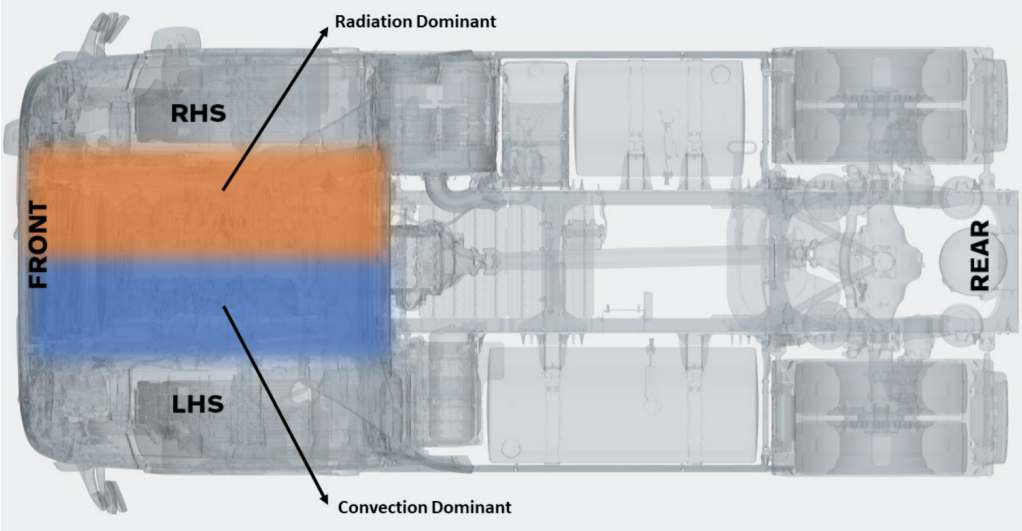

Figure 1.3: Distribution of heat transfer dominance in the under-hood region of a truck

Each component in the under-hood region adds to the thermal mass of the domain. The thermal mass plays a significant role in the under-hood thermal environment

behavior in heavy loading conditions or thermal soak where the heat rejection out of the system is limited. When the engine is turned off, so too is the engine fan that displaces the air within the under-hood. Without the forced convection pushing the heated air out of the under-hood, the heat rejection is substantially reduced. The thermal mass and thermal energy in the under-hood in a such a thermal soak condition can lead to higher temperatures in the under-hood than when the engine fan is engaged. This effect could potentially lead to component overheating and failure. A schematic depiction of the under-hood is shown in Figure 1.4.

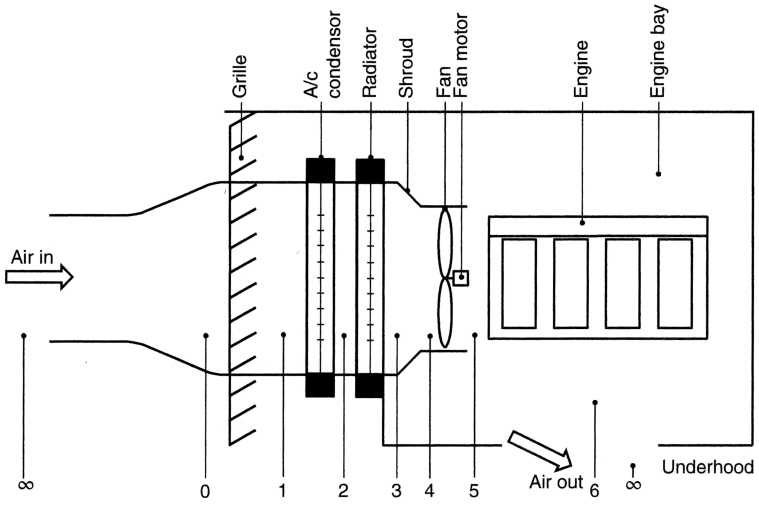

Figure 1.4: Under-hood schematic depicting air in and out of the under-hood environment [11]

The large gradient of temperature and different modes of heat transfer (i.e. conduction, convection, and radiation) in the under-hood region makes it complex and challenging to understand. The thermal environment of such a complex domain is dependent on various factors such as the ambient temperature, road conditions, engine operating condition, fan engagement strategy etc. An intense drive cycle may include large variations in geographical terrain or other conditions that require extreme engine operating conditions. This would result in increased loading on the cooling system and subsequently hotter air entering the under-hood. It becomes of utmost importance to build a methodology to simulate and model the heat transfer phenomena in a efficient manner and attain realistic results. This will enable intelligent future design, ensuring that components operate within their optimal temperature ranges, preventing overheating and are therefore more durable.

1.5 Limitations / Demarcations

In an effort to limit the scope of the project such that sufficient work may be performed within the stipulated duration, a base simulation model was provided that included the resolved study of cooling system performance and air flow in the under-hood region. The internal flow and thermal environments inside the powertrain components were not resolved in the simulation. Instead, temperature and convective

boundary conditions based on test results and previous simulation experience were provided as inputs to the simulation to model the powertrain components. Given the time available, only critical under-hood components were included in the solid domain. The simulation was also restricted to steady-state operating conditions. Lastly, parts of the results have not been included in this report citing confidentiality. This includes absolute values of monitored parameters in plots. All simulations were carried out in STAR-CCM+ version 2310.

2

Theory

Computational Fluid Dynamics (CFD) is a computational tool which uses numerical methods to analyze the fluid flow and heat transfer by discretizing the domain under study. Discretization is the process of transforming the domain and continuous governing equations into discrete form by dividing the domain into finite number of control volumes. The Finite Volume Method (FVM) is one of the common methods of discretization. The governing equations are solved across these control volumes. Conservation of mass, momentum and energy constitute the governing equations of fluid flow. The conservation of mass and momentum equations are partial differential equations which describe the motion of viscous fluid substances. These equation together are known as Navier-Stokes equations.

2.1 Governing equations of Fluid Dynamics

Equation (2.1) states the general transport equation expressed in form of Partial Differential equation (PDE), where ϕ represents any state variable either in vector form such as velocity or scalar form such as temperature [12]. This general form of representation of transport equation is used to express conservation of mass, momentum and energy.

$$\frac{\partial(\rho\phi)}{\partial t} + u_j \frac{\partial \rho\phi}{\partial x_j} = \frac{\partial}{\partial x_j}(\Gamma \frac{\partial \phi}{\partial x_i}) + S_\phi \tag{2.1}$$

2.1.1 Continuity

The continuity equation is the fundamental concept that represents the conservation of mass in fluid flow. It is given according to equation (2.2), where ρ represents the density of the fluid, v_i represents the i component of the velocity vector and x_i denotes the spatial coordinates. For an incompressible flow, density ρ = constant.

$$\frac{d\rho}{dt} + \rho \frac{\partial v_i}{\partial x_i} = 0 \tag{2.2}$$

2.1.2 Momentum

The momentum equation represents the behavior of a fluid under the influence of various forces. This is given according to equation (2.3), where σ_{ij} is the stress tensor and f_i represents the body forces.

$$\frac{d\rho v_i}{dt} = -\frac{\partial P}{\partial x_i} + \frac{\partial \tau_{ji}}{\partial x_j} + \rho f_i \tag{2.3}$$

Stress tensor σ_{ij} is given according to equation (2.4) shown below, where, p is the pressure acting normal on the fluid element and τ_{ij} is the viscous stress tensor. δ_{ij} represents Kronecker delta which takes value of 1 when $i = j$ and takes the value of 0 when $i \neq j$.

$$\sigma_{ij} = -p\delta_{ij} + \tau_{ij} \tag{2.4}$$

Viscous stress term is given according to equation (2.5)

$$\tau_{ij} = 2\mu S_{ij} - \frac{2}{3}\mu S_{kk}\delta_{ij} \tag{2.5}$$

where μ is the dynamic viscosity, S_{ij} the strain rate tensor. The stress tensor σ_{ij} is given in equation (2.6)). The second and third term on the right side of the equation are the viscous stress tensor terms.

$$\sigma_{ij} = -P\delta_{ij} + 2\mu S_{ij} - \frac{2}{3}\mu S_{kk}\delta ij \tag{2.6}$$

2.1.3 Energy

The energy equation is derived on the basis of first law of Thermodynamics according to which the rate of change of energy is equal to the summation of rate of heat added to or removed from the system and the rate of work done. Heat added to a system under study can be defined by $\nabla.\mathbf{q}$ and the work done is given as the product of all the forces with the velocity vector influencing motion. Energy equation is given according to equation (2.7),

$$\frac{\partial \rho E}{\partial t} + \frac{\partial(\rho E v_j)}{\partial x_j} + \frac{\partial p v_j}{\partial x_j} - \frac{\partial(v_i \tau_{ij})}{\partial x_j} + \frac{\partial q_j}{\partial x_j} = \rho\varepsilon + S_u \tag{2.7}$$

where, E is the total energy, q_i is the heat flux, ε is any internal heat source, σ_{ij} is the stress tensor and S_u is the energy source term. Energy in solid bodies on a macro scale is represented by enthalpy as there is no motion or momentum of the body and the rate of increase of energy is equal to the added heat. Total energy can represented in terms of pressure and enthalpy as shown in the equation (2.8), where H is the total enthalpy.

$$E = H - \frac{p}{\rho} \tag{2.8}$$

2.1.4 Turbulence Modeling

Complex flow characterized by irregular fluctuations and eddies of different lengths and time scales are classified as turbulence. It occurs when the intertial forces experienced by the fluid is larger than the viscous forces. Modeling turbulence in thermal simulations is important especially when the convection is one of major modes of

heat transfer in the domain under study. Due to the complex nature, large scale of simulations and limited time and computational resources in automotive industries. Turbulence is modeled using Reynolds Averaged Navier Stokes (RANS) approach within this study rather than more computationally expensive turbulence resolving models such as variations of LES.

RANS models are initially categorized by the decomposition of a transport variable into mean and fluctuating components as shown in equation (2.9) below.

$$\phi = \bar{\phi} + \phi' \tag{2.9}$$

Time averaging through equation (2.10):

$$\overline{\phi} = \frac{1}{2T}\int_{-T}^{T} \phi dt \tag{2.10}$$

and inserting the decomposition of velocity into the governing equations results in a new set of equations with an additional term appearing within the momentum and energy transport equations. This additional term is known as the Reynolds stress tensor, and must be modeled in terms of mean flow quantities in order to provide closure of the initial governing equations [13]. These equations are shown in equation (2.11) below.

$$\begin{aligned}
\frac{\partial \rho}{\partial t} + \frac{\partial \rho \overline{v_i}}{\partial x_i} &= 0 \\
\frac{\partial \rho \overline{v_i}}{\partial t} + \frac{\partial \rho \bar{v}_i \bar{v}_j}{\partial x_i} &= -\frac{\partial \overline{p}}{\partial x_i} + \mu \frac{\partial^2 \overline{v_i}}{\partial x_j \partial x_i} - \frac{\partial \rho \overline{v_i' v_j'}}{\partial x_j} + f_i \\
\frac{\partial}{\partial t}(\rho \overline{E}) + \frac{\partial \rho \bar{E} \bar{v}_i}{\partial x_i} &= -\frac{\partial \overline{p}_{mod} \overline{v_i}}{\partial x_i} + \mu \frac{\partial^2 \bar{v}_i \bar{v}_k}{\partial x_j \partial x_i} - \frac{\partial \rho \bar{v}_k (\overline{v_i' v_j'})}{\partial x_j} - \frac{\partial \overline{q_i}}{\partial x_i} + f_i v_j
\end{aligned} \tag{2.11}$$

Introducing a concept of turbulence eddy viscosity, μ_t, allows for such a closure through a set of assumptions known as the Bousinessq Assumption. There resulting simplification of is seen in equation (2.12) below.

$$\rho \overline{v_i' v_j'} = -2\mu_t \bar{s}_{ij} + \frac{2}{3}\delta_{ij} k \tag{2.12}$$

where $\bar{s}_{ij}$ is the mean strain rate tensor, k is turbulence kinetic energy defined as

$$k = \frac{1}{2}\overline{v_i' v_i'} \tag{2.13}$$

and δ_{ij} is the Kronecker delta. This approximation leads to a two-equation closure model, of which the two most commonly implemented are variations on the k-ϵ model, and the k-ω model. These two-equation models solve for the transport of turbulence kinetic energy and turbulent dissipation in order to resolve turbulence.

In selecting a k-ϵ model in STAR-CCM+, the selection defaults to the Realizable Two-Layer model. This model implementation has been developed based on two

variations of the standard k-ϵ model, or SKE: the Two-Layer approach first proposed by Rodi [14] to better model the viscous sub-layer and buffer layer, and the Realizable $k-\epsilon$ model first proposed by Shih et al [15]. In selecting a $k-\omega$ model, where $\omega \propto \epsilon/k$, STAR-CCM+ defaults to an SST $k-\omega$ model implementation derived from the SST model presented in Menter [16]. Further information on specifics of the STAR-CCM+ implementation, including equation expansion and coefficient values, can be found in the User Guide [17].

2.2 Heat Transfer

2.2.1 Conduction

Conduction is a contact based heat transfer phenomena where the heat is transferred within and between contacting bodies. Conduction is given according to Fourier Law in which the temperature gradient is linear in homogeneous materials. The equation is given below in equation (2.14)), where the local heat flux vector is $\dot{\mathbf{q}}''$, k is the thermal conductivity, and $\nabla(\mathbf{T})$ the temperature gradient.

$$\dot{\mathbf{q}}'' = -k\nabla(\mathbf{T}) \tag{2.14}$$

2.2.2 Convection

Convection is a mode of heat transfer in which the heat is transferred between a solid and fluid medium due to currents of the moving fluid. The general analytical form of convective heat transfer is given according to equation (2.15))

$$\dot{\mathbf{q}}_s'' = h(T_s - T_{ref}) \tag{2.15}$$

where $\dot{\mathbf{q}}_s''$ is the heat flux at the contact surface between fluid and solid, h is the convective heat transfer coefficient, T_s is the surface temperature, and T_{ref} is a characteristic temperature of the fluid moving over the surface. Heat transfer coefficient is representative of the resistance to convective heat transfer between the fluid and the solid medium.

Convection can be either natural or forced depending on the nature of force that causes variations in the fluid currents. In natural convection, fluid motion is caused by buoyancy resulting from the variations in density of the fluid caused by local temperature gradients. In forced convection, the fluid motion is caused by external sources such as a fan or propeller.

2.2.2.1 Heat Transfer Coefficient

Heat Transfer Coefficient (HTC) is a critical value within the solver. HTC is a constant of proportionally that relates $\dot{q}_s''$, T_s, and T_{ref}. While the first two parameters - $\dot{q}_s''$, T_s - are well defined within a system, there is typically some latitude in the selection or determination of T_{ref}. The surface flux is calculated after cell temperature and/or wall temperature is solved through the energy equation. From equation

(2.15), an infinite number of various of HTC and T_{ref} exist that satisfy the equation.

The primary method by which HTC and T_{ref} are resolved in STAR-CCM+ is through utilizing local cell and wall temperature values to determine a Local Heat Transfer Coefficient. This method uses the wall-face centroid temperature values of a cell adjacent to a wall as T_{ref} value as seen in equation (2.16)

$$h_{local} = \frac{\rho_f(y_c)C_{p,f}(y_c)u_\tau}{T^+(y^+(y_c))} \tag{2.16}$$

where ρ_f is the fluid density, $C_{p,f}$ is the fluid-specific heat capacity, u_τ is a velocity scale based on wall shear stress, T^+ is dimensionless temperature, y^+ is a dimensionless wall distance, and y_c is the normal distance of the near-wall cell in which the other values are determined [17].

Using h_{local}, a local reference temperature can be calculated from equation (2.17) below.

$$T_{ref,local} = T_s - \frac{q_s''}{h_{local}} \tag{2.17}$$

2.2.2.2 Dimensionless Parameters

Several dimensionless parameters have been developed to assist in qualifying the types of convective heat transfer, particularly, Rayleigh Number *Ra*, Prandtl Number *Pr*, and Reynolds Number *Re*. These are defined in this section.

Reynolds Number

Reynolds number is defined as the ratio of inertial forces to the viscous forces acting on the fluid. It is defined as shown in the equation (2.18)) where ρ is the fluid density, v is the velocity, L is the characteristic dimension and μ is the kinematic viscosity [18].

$$Re = \frac{\rho v L}{\mu} \tag{2.18}$$

Grashof Number

Grashof number is a parameter which is given as the ratio of buoyant forces to viscous forces. It is given as shown in equation (2.19), where g is acceleration due to gravity, β is coefficient of volume expansion, T_s is the surface temperature, T_∞ is the bulk temperature, L is the characteristic length and ν is the kinematic viscosity.

$$Gr = \frac{g\beta(T_s - T_\infty)L^3}{\nu^2} \tag{2.19}$$

Prandtl Number

Prandtl number relates the viscosity of the fluid with its thermal conductivity correlating the momentum transport and thermal transport respectively. It is given as

the ratio as expressed in equation (2.20)), where ν is the dynamic viscosity and α is the thermal conductivity. Thermal conductivity of the material is defined as the ability of the material to conduct heat [18].

$$Pr = \frac{\text{Thermal diffusivity}}{\text{Momentum diffusivity}} = \frac{\nu}{\alpha} \tag{2.20}$$

Rayleigh Number

Rayleigh number quantifies the natural convection in a given system. It is given as the product of Grashof number and Prandtl number.

$$Ra = Pr * Gr \tag{2.21}$$

The domination of the type of convective heat transfer can be quantified using the relation shown in table the below.

$GrRe^2 >> 1$	Natural convection dominates and forced convection is neglected
$GrRe^2 << 1$	Forced convection dominates and natural convection is neglected
$GrRe^2 \approx 1$	Both natural and forced convection is considered

2.2.2.3 Boundary Layer

The layer of fluid in the vicinity of the bounding surface is known as the velocity boundary layer where, due to shear stress, the velocity of the fluid is reduced significantly relative to the free stream. The flow in this region is dominated by the viscous forces. It is important to have a high resolution mesh in this region in order to capture the influence of viscous force on the velocity flow field. A typical thermal boundary layer is formed when the fluid flows across a surface with a relatively higher temperature. The fluid that is in contact with the surface achieve equilibrium at the surface's temperature. This layer of fluid then exchanges energy with the adjoining fluid layer, resulting in a temperature gradient. This region of fluid where the temperature gradient exists is known as thermal boundary layer.

Similar to velocity boundary layer, it is equally important to capture the thermal boundary layer effect. In order to the boundary layer effect, it is necessary to have appropriate number of cells to resolve the boundary layer thickness. Boundary layer thickness is defined as the distance from the wall to the point where the velocity and temperature reach 99% of the free-stream values. The fluid and thermal boundary layer are shown in figure 2.1.

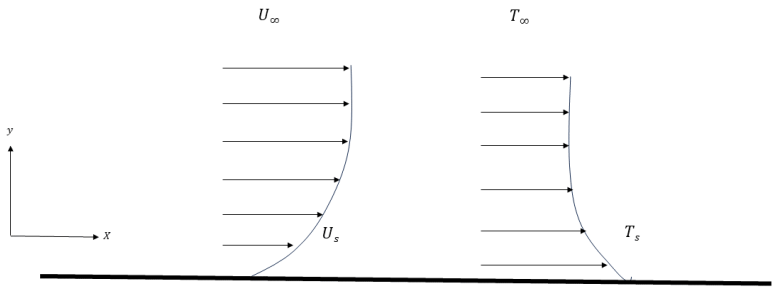

Figure 2.1: Velocity and Thermal boundary layer

2.2.3 Radiation

Radiation is a surface phenomena in which the heat transfer takes place due to the difference in the energy states of photons. This difference in energy states of photons is typically caused by a large temperature gradient between two or more surfaces. Incident radiation is termed as irradiation, and is defined for perfectly absorptive body, known as a black body as in equation (2.22) below.

$$G_{bb} = q_{bb} = \sigma T^4 \tag{2.22}$$

The intensity of power emitted depends on the absorptivity, transmisivity and reflectivity of the surface:

- Absorptivity is the fraction of irradiation that is absorbed by the surface. It is denoted by α.
- Reflectivity is the fraction of irradiation reflected from the surface. It is denoted by ρ.
- When the surface is semi-transparent, a fraction of irradiation is absorbed and transmitted through the surface. This is known as transmissivity and denoted by τ.

$$\alpha + \rho + \tau = 1 \tag{2.23}$$

For a black body, $\alpha = 1$. The sum of absorptivity, reflectivity and transmissivity is one for any given surface is as shown in equation (2.23). The solver multiplies the radiative heat flux with emissivity. Emissivity is the ratio of power emitted by the body to the power it would emit as a black body. The value of emissivity is between 0 and 1.

The emitted radiative heat flux is given by q_e as shown in equation (2.24), where σ is the Stefan-Boltzmann constant, T is temperature.

$$q_e = \epsilon q_{bb} = \epsilon \sigma T^4 \tag{2.24}$$

2.2.4 Surface-to-Surface Radiation

Surface-to-surface radiation is a method of modeling the radiative interaction between bodies numerically for which radiating and absorbing surfaces are accounted without an intermediate medium. This means that the intermediate medium, either a transmissive solid or fluid, does not participate in absorbing, scattering or reflecting the radiation. This method uses view factors. View factor in radiation is denoted by F_{ij} and is a geometric metric defining the fraction of the radiation leaving surface i that is intercepted by surface j. The analytical equation of view factor between two arbitrary surfaces is given by equation (2.25). View factors obey the law of reciprocity, i.e. $A_i F_{ij} = A_j F_{ji}$ and the sum of view factors is 1 following the summation rule as shown in equation (2.26).

$$F_{i \to j} = \frac{1}{A_i} \int_{A_i} \int_{Aj} \frac{cos\theta_i cos\theta_j}{\pi S^2} dA_j dA_i \tag{2.25}$$

where S is the length of a line connecting two arbitrarily oriented surfaces, A is the area of the surface, and θ represents the polar angles that line S creates with respective surface normal vectors for either surface.

$$\sum_{j=1}^{N} F_{ij} = 1 \tag{2.26}$$

where N is the number of surfaces. Surface-to-surface radiation models are dependent on spatial discretization of the surface to generate radiation patches. These patches act as respective surfaces from which view factors are calculated. Gray Thermal radiation is considered which solves radiation independently of wavelength while also enforcing Kirchhoff's law (equal emissivity and absorptivity) by requiring the sum of the emissivity, reflectivity, and transmissivity to be 1.0 at surfaces. An assumption made by this model is that the radiation is diffuse i.e. both emissivity and absorptivity are independent of both wavelength and direction. Such a surface is termed as a diffuse gray surface. It is a common method used in most of the engineering applications to reduce the computational complexity and to simplify the mathematical treatment of radiative heat fluxes.

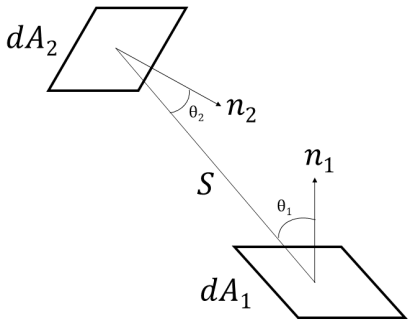

Figure 2.2: View Factor

Radiosity is defined as the total radiative heat flux leaving the surface which includes both the emitted and reflected radiative heat flux. It is represented as J and given according to equation (2.27)

$$J = q_e + \rho G \quad = \quad \epsilon_i E_{bb} + (1 - \epsilon_i) G_i \tag{2.27}$$

where q_e is the emitted radiative heat flux, ρ is surface reflectivity and G is the total incident radiation - irradiation. The net radiation exchange at a surface is given by equation (2.28)

$$q_i = A_i(J_i - G_i) \tag{2.28}$$

where A_i is the area of surface i, J_i is the radiosity at surface i and G_i is total incident radiation on surface i. The above equation can be further simplified as shown below.

$$q_i = A_i(E_i - \alpha_i G_i) q_i = A_i \left(J_i - \frac{J_i - \epsilon_i E_{bb}}{1 - \epsilon_i} \right) \tag{2.29}$$

$$q_i = \frac{E_{bb} - J_i}{(1 - \epsilon_i)/\epsilon_i A_i} \tag{2.30}$$

The net radiation exchange between the surfaces can be expressed as the irradiation received by the surface (surface1) must be equal to the sum of radiosity from the surfaces that are seen by the surface 1. This is given as shown in equation (2.31)

$$A_i G_i = \sum_{j=1}^{N} F_{ij} A_j J_j \tag{2.31}$$

2.2.5 Conjugate Heat Transfer

Conjugate Heat Transfer is a coupled multiphysics approach where the temperature state variable is solved in the fluid and solid continua, and pressure and velocity are solved in the fluid continua. The communication between the fluid and solid continua takes place in the solver through interfacing. The solid region is governed by conservation of energy and the fluid region by both Navier-Stokes equation and

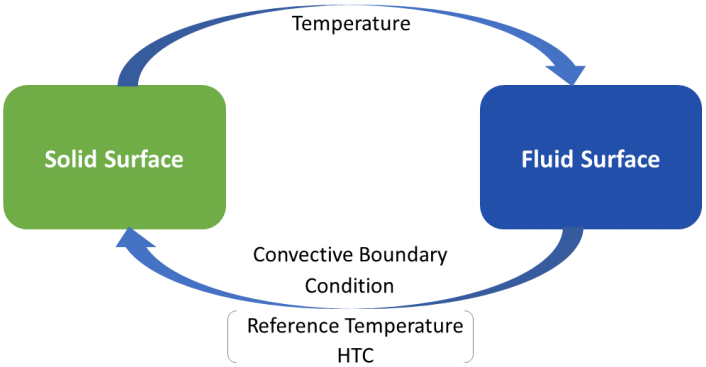

Figure 2.3: Exchange of state variable in CHT

the energy equation. This is represented in figure 2.3. The fluid solver resolves convection. The resolved local reference temperature and heat transfer coefficient are mapped to the solid solver as convective boundary conditions. The solid solver uses these values as boundary conditions to resolve external surface temperature, which is then mapped back to the fluid solver. The fluid solver uses this corrected solid surface temperature to more accurately resolve the convective boundary conditions, and the iterative process continues the communication until a converged solution is reached.

Heat exchange between the solid surface with internal heat conduction and external fluid passing over it is an example of conjugate heat transfer. The heat transfer within the solid is governed by the heat conduction equation, while the heat transfer within fluid is governed by continuity, momentum and energy equations [19]. At high surface temperatures, radiation plays an important role in the heat transfer between solid surfaces. Radiation and conduction mode of heat transfer is solved in the solid continuum.

2.2.6 Mesh Interfacing

In typical CHT models, each participating continuum requires a dedicated mesh. These meshes must be connected in order to communicate information such that the total domain can be solved. STAR-CCM+ provides multiple methods in which data may be transferred across these mesh interfaces. The primary methods investigated in this work are STAR-CCM+'s contact interfacing and data mappers. The theory of these methods differs notably.

In STAR-CCM+, contact interfacing can be summarized with three distinct methods: a conformal interface, an indirect or imprinted interface, or a mapped contact interface. In the case of a conformal interface, this would translate to the perfect connection of two faces where the cell vertices are aligned. Where conformal inter-

faces are not possible, STAR-CCM+ allows for either imprinting a contact interface, aligning the boundary faces without necessarily aligning the vertices, or mapped contact interfaces, where the faces will be virtually connected based on tolerance settings.

It is understood that STAR-CCM+'s contact interfacing acts as a direct information transfer between the two boundaries representing the interface. For a conformal interface, this information exchange is straight forward as values from one mesh are directly transferred to another without the need for interpolation. However, for indirect or mapped interfaces where cell vertices and centroid nodes may not be aligned. STAR-CCM+ interpolates or otherwise determines the value of the scalar fields transferred between faces.

Data mappers, the second primary method investigated, explicitly uses interpolation techniques to exchange user specified scalar field values. STAR-CCM+ offers various interpolation techniques to map data between vertices, faces, or cells. The two techniques investigated in this work are Nearest Neighbor and Shape Function interpolations. These methods use data calculated from a source entity, i.e. a vertex, face, or cell, as well as a target entity. An example of this can seen in figure 2.4 below, with face $\boldsymbol{n}$ in red as the target, and face $\boldsymbol{k}$ in blue as the source.

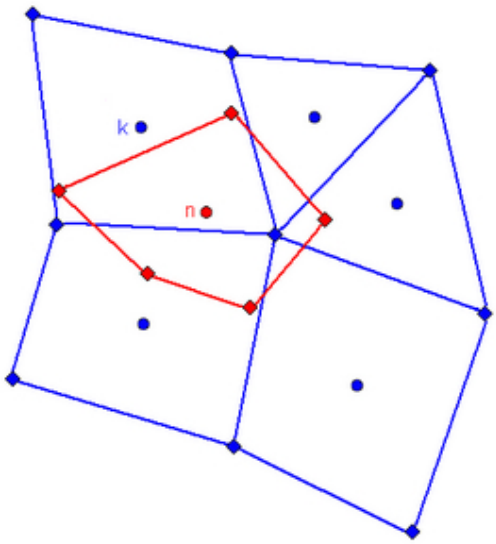

Figure 2.4: Representation of two distinct mesh faces overlapping to depict an interface. Image taken from STAR-CCM+ User Guide

The operation of the Nearest Neighbor technique simply maps the nearest source value to the target of interest. In reference to figure 2.4, for a face-to-face mapping, nearest neighbor would result in face $\boldsymbol{k}$ being mapped to face $\boldsymbol{n}$. This method is fast as only simple distance calculations around the target face need to be performed.

Shape Function interpolation is a commonly used technique when performing finite element analysis or otherwise communicating data to or from a finite element mesh. The technique uses the vertex data of source face, $\boldsymbol{k}$, and interpolates the solution to the target face, $\boldsymbol{n}$, using the nodal shape functions in equations (2.32) and (2.33)

$$\boldsymbol{f}_n = \sum_{l \in N(k)} f_l N_l(\xi_n, \eta_n, \chi_n) \tag{2.32}$$

$$\begin{aligned} N_1 &= \frac{(1-\xi)(1-\eta)}{4} \\ N_2 &= \frac{(1+\xi)(1-\eta)}{4} \\ N_3 &= \frac{(1+\xi)(1+\eta)}{4} \\ N_4 &= \frac{(1-\xi)(1+\eta)}{4} \end{aligned} \tag{2.33}$$

N_l denotes the shape function at vertex l, f_l denotes the solution value at vertex l, and (ξ_n, η_n, χ_n) denote the local coordinates of point $\boldsymbol{n}$ within element $\boldsymbol{k}$. The sum is taken over the set of vertices within element $\boldsymbol{k}$ [17].

3
Methods

This chapter describes the process of developing the simulation framework/methodology along with supportive studies with simplified geometries performed to better understand key parameters of the simulation model.

3.1 Geometry

Three primary ways to import geometry into STAR-CCM+ were explored. These methods consisted of: first, generating STL files to be imported as STAR-CCM+ 3D-CAD Parts; second, generating NASTRAN .nas mesh files to be imported as Parts; and lastly, generating either a NASTRAN, a .ccm STAR-CCM+ mesh specific, or other CAE model files to be imported as a CAE model into the STAR-CCM+. The second option was selected through experimentation as this approach of importing mesh data as Parts had two primary benefits over the other methods. The first benefit is that the .nas files were considerably smaller in file size than .stl files. This was beneficial both for the local storage of the component geometric data, but also in limiting the additional data stored within the STAR-CCM+ .sim file after importing. This reduces the total simulation size and required processing power to handle simulation setup and debugging. The second benefit is that having the components accessible as Parts is desirable as they can then be used within STAR-CCM+'s robust meshing pipeline, which offers key features such as automated interface generation or the attached shell creator (found in version 2402 or later).

3.1.1 Pre-processing

In an ideal scenario, all simulation geometry would be completely "clean", meaning all tessellation data perfectly aligns. This, however, is rare throughout the industry as geometric designs are often generated independently from one another and might have been created using differing software packages. As a result, geometry must typically be processed before it can be used to generate a mesh. This is referred to as geometry Pre-processing.

Pre-processing for this work was performed using BETA CAE's ANSA Preprocessor. ANSA provides powerful pre-processing utilities, allowing a user to quickly remove unnecessary geometric details such as company logos, fasteners, or other highly detailed facets that introduce needless complexity. Along with these details,

any unnecessary inner or duplicate surfaces are removed during pre-processing, and additional surfaces are generated to close free edges or repair corrupted surface data.

During the pre-processing stage, a user can modify the simulation geometry to such a level that an ideal mesh can be generated. Across the industry, however, this level of preprocessing is generally understood to be too costly in terms of engineering man-hours. Instead, additional meshing utilities, such as surface wrapping, are used to overcome minor geometric issues after an initial cleaning pass of the geometry. These meshing utilities will be discussed in section 3.2.1 later within this chapter.

To better organize the large number of components within the under-hood, the ANSA Model Browser was used for creating part assemblies roughly representing unique systems within the under-hood. Some of the groups that were created are exhaust assembly, engine assembly, air inlet assembly, transmission gearbox, and so on. Several key assemblies are shown below in figures 3.1 to 3.5.

Engine Assembly

The geometry in the engine assembly comprises the engine block, valve cover, oil sump, and cylinder head.

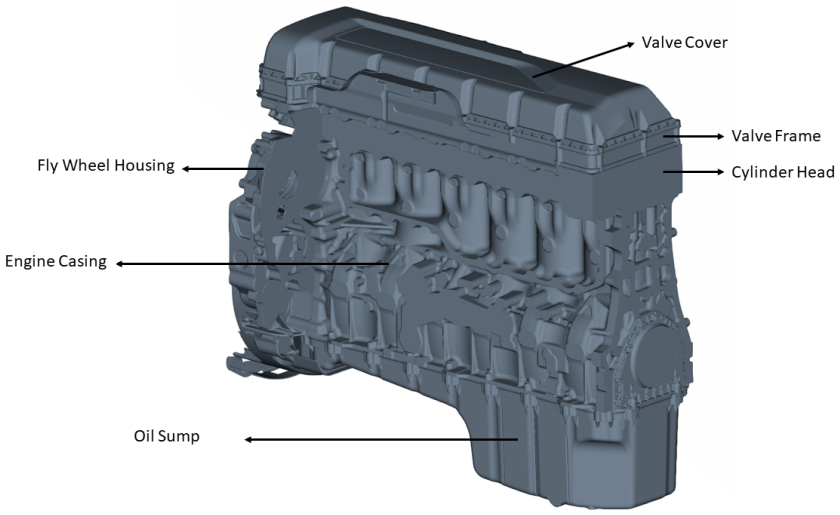

Figure 3.1: Engine Assembly

Exhaust Assembly

The exhaust system comprises the exhaust manifold, turbo compound, butterfly valve and down-pipe, as shown in figure 3.2. This region is radiation-dominant due to the high temperature of exhaust gas handled by the components.

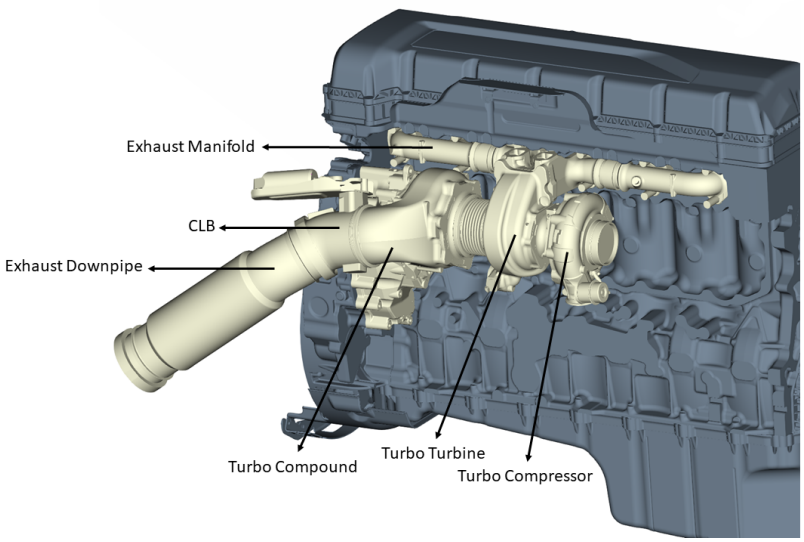

Figure 3.2: Exhaust Assembly

Exhaust Gas Recirculation Assembly

Components such as exhaust gas recirculation valve, cooler and connecting pipes are grouped under exhaust gas recirculation assembly, as shown in figure 3.3

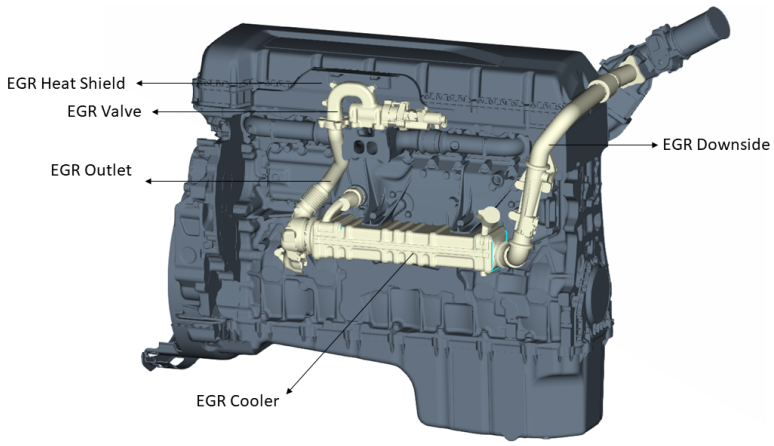

Figure 3.3: Exhaust Gas Recirculation Assembly

Air Intake Assembly

The solid modeled air intake system included ducting for fresh air, the primary air filter, through the turbo compressor charging the air. The engine air intake is then also included in this subdivision, along with the air throttle valve and EGR inlet. These can be seen in figure 3.4 below.

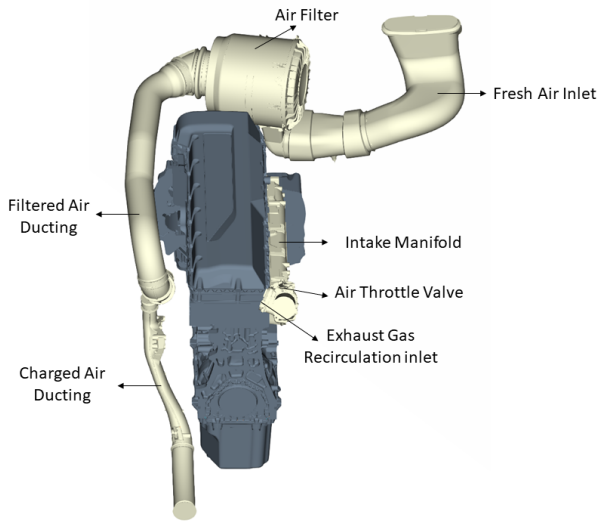

Figure 3.4: Air Intake Assembly

Auxiliary Components

The components in and around the engine such as starter motor, air valve unit, oil filter, and fuel filter housing are grouped under auxiliary assemblies due to their varied functionalities. These components are shown in figure 3.5.

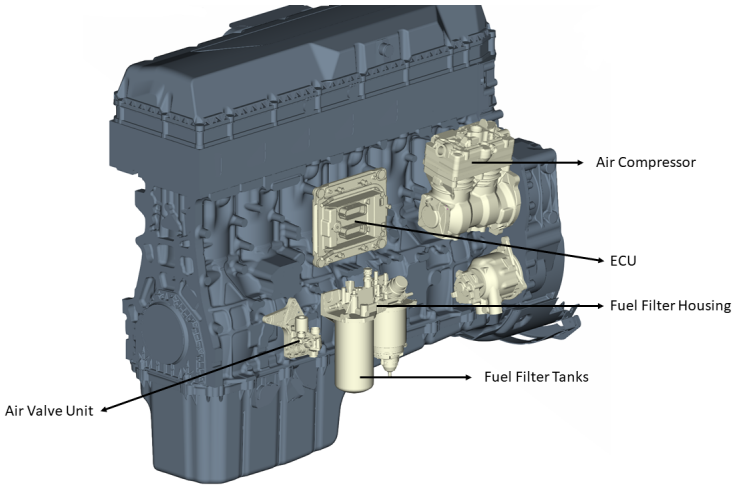

Figure 3.5: Engine Auxiliaries Components

3.1.2 Computational Domain

The domain to be simulated includes the entire truck situated within an rough reconstruction of the local climatic wind tunnel at Volvo GTT in Gothenburg. A schematic representation of the computational domain is shown in Figure 3.6 below. This representation has removed all details of the modeled wind tunnel to protect confidental information. The domain consists of an inlet and an outlet shown in the

green and blue respectively.

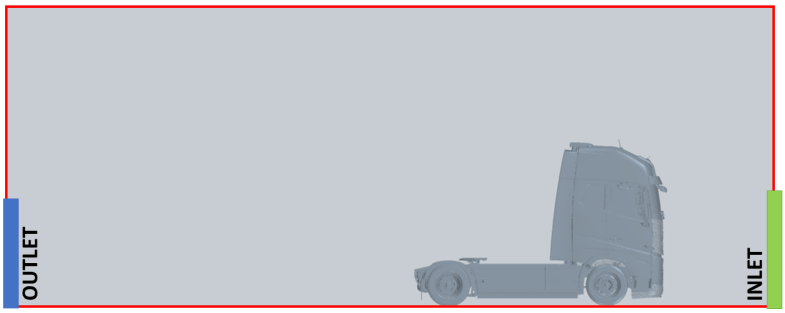

Figure 3.6: Representative Computational Domain

3.2 Meshing

Meshing is one of the crucial aspects of any simulation. Various factors are taken into consideration while volume meshing both solid and fluid regions. Solid regions can either be meshed as a shell, or as a solid body, and individual components may be meshed uniquely depending on resolution needs. In a thermal simulation, the mesh shape of solid components is less critical than aspect ratio, aiming for higher resolution along direction of energy flow. For fluid meshes, however, the cell shape may introduce an amount of interpolation errors and numerical diffusion depending on the flow characteristics. Furthermore, it is desirable to avoid interfaces arising from having multiple mesh configurations in the same geometric domain unless it is demanded by the solver for any specific purpose. Such interfaces introduce additional numerical errors due to interpolation of solution data.

3.2.1 Operations

Surface Wrapper

Additional meshing utilities are used to overcome minor geometric deficiencies that had not been rectified during pre-processing. One such utility offered in STAR-CCM+ is the Surface Wrapper. This meshing operations generates a new surface mesh around the geometry of interest, which can then be used to generate a finite volume meshes within or around the surface wrapped geometry. Surface wrapping has been found to be a critical meshing operation to reduce the amount of pre-processing required to allow for the generation of a finite volume mesh. Upon importing relatively clean geometry, all non-shell parts are universally surface wrapped before generating a volume mesh.

Shell Meshing

Another such utility to address minor geometric deficinies is STAR-CCM+'s Shell Mesher. Similar to the Surface Wrapper, the Shell Mesher generates a new surface mesh around the geometry. This mesh splits the new surface into two separate faces, a front and a back, and applies a user specified virtual thickness between them when implemented into the solver. This allows for the reduction of cells within a domain rather than needing to model every component with 3D cells. In the simulations performed as a part of this work, components that have generally uniform thickness, i.e. pipes and ducts, were meshed as shells.

Automated Meshing

Different meshers and options were selected to obtain separate surface wrappers for components used in solid and fluid continua. Geometry was wrapped in such a way that the fluid continua captured all parts of the domain with air flow, and the solid continua captured all component fluid-facing surfaces. The key benefit of this is that the unneeded or problematic internal and intersecting surfaces in the fluid continua are not captured and are then ignored. A leak detection test is performed for selective components by placing multiple seed points to ensure that the surface wrapper is free of voids and cracks. The surface wrapped geometry is then volume meshed.

A Polyhedral mesher is chosen for both fluid and solid continua. Prism layers were used in the fluid region to capture the boundary-layer effects on the walls. Quadrilateral mesher is used to generate the shell mesh.

3.2.2 Wall y+

The dimensionless distance in the wall normal direction in the flow domain, known as wall y^+, is an important parameter to describe the boundary layer. It represents the distance from center of the first cell to the wall. In order to capture and resolve the flow in the near wall region, it is important to have the value of y^+ within the viscous sub-layer. It is given according to equation 3.1, where y is the distance from the wall to the center of first cell, v_t is the friction velocity and ν is kinematic viscosity of the fluid.

Upon using two layer $k-\epsilon$ turbulence model, the all wall $y+$ function is used. This function enhances the near wall region simulation and ensures that flow close to the wall is better resolved than using the logrithmic wall function. This is achieved in this project by ensuring that the value of $y+$ in the under-hood region is well below 1. This is shown in figures 3.7 to 3.9. Distribution of wall $y+$ on the external surfaces of the truck is shown in figure 3.10.

$$y^+ = \frac{y v_t}{\nu} \tag{3.1}$$

Figure 3.7: $y+$ value distribution in the under-hood region of the truck - LHS

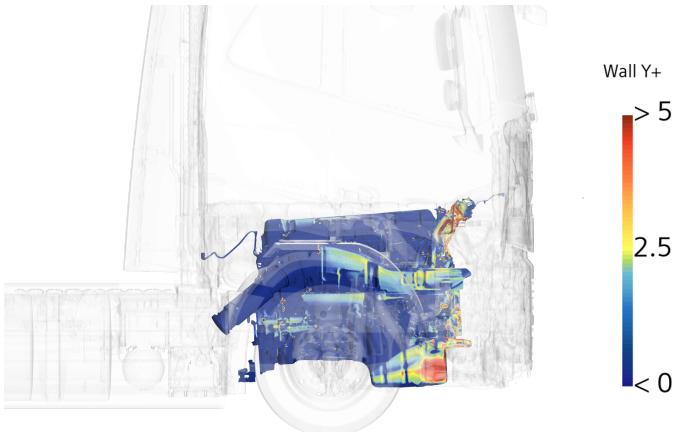

Figure 3.8: $y+$ value distribution in the under-hood region of the truck - RHS

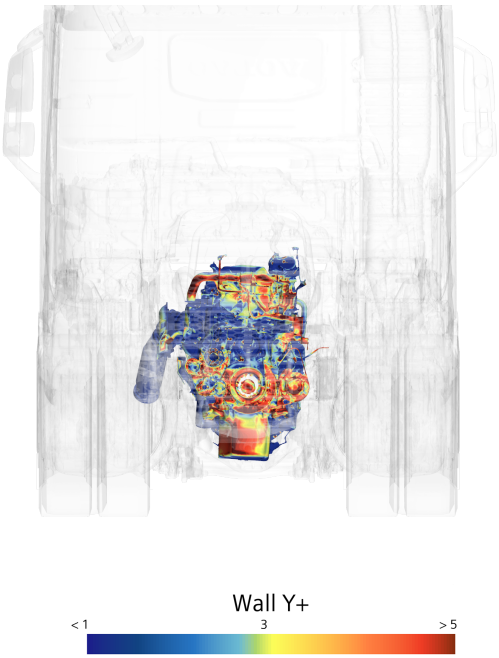

Figure 3.9: $y+$ value distribution in the under-hood region of the truck - Front

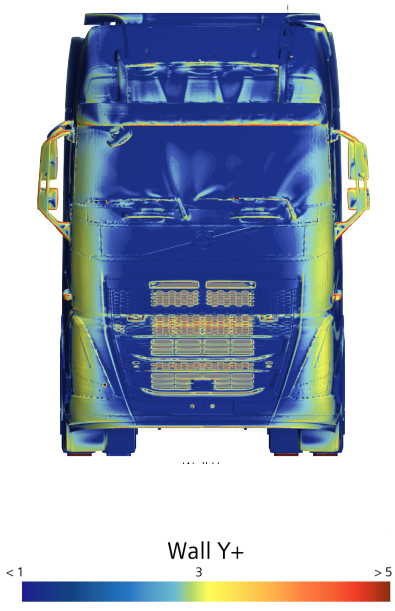

Figure 3.10: $y+$ value of complete truck

3.3 Continua Interfacing

The method in which data is communicated within the model is further explored in this section. The quality of a CHT model is dependent on the quality of the interfaces between the two interacting continua. A CHT study with simplified geometry was performed to understand the influence of mesh parameters on the quality of interface between the fluid and solid continua, and on the data mapped across the interface.

A simple domain was modeled with a single component in the solid domain. A component with a complex geometry was chosen with the idea being to have some poor quality mesh cells which, in turn, would affect the quality of the interface. Through basic investigation, it was determined that the primary TC turbine satisfies this criterion as the curvature of the surface introduced complexity when interfacing with a surrounding fluid mesh. A visualization of the domain can be seen in figure 3.11.

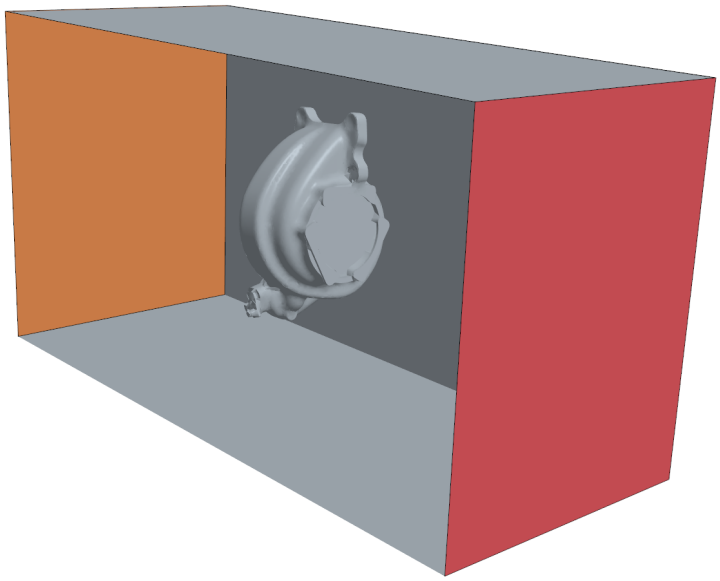

Figure 3.11: Domain of the study used to better understand STAR-CCM+ interfaces versus Data Mappers

The domain setup consisted of an inlet and an outlet on either side of a block, with the turbine located approximately in the center. The turbine was modeled as a shell for two reasons. Firstly, the meshing of a shell required only a surface mesh, reducing the computational burden of the mesh operation. Secondly, the shell mesher can utilize a quadrilateral element shape. The difference in shape between the solid surface, the surface wrap, and the fluid wrap will provide the worst-case-scenario for this analysis. A constant specified heat source of 1000 W was applied to the back surface of the shell, which represents the inner surface of the TC assembly. This surface is in contact with the hot exhaust in the original model. The shell

thickness considered is 1 mm for this simplified study. STAR-CCM+ considers shell thickness purely virtually, so the surface area of the front and back faces of the shell are equal. The material conductivity was increased to 1000 W/mk. The component and domain are then surface wrapped, which is then used to generate an automated mesh for the fluid domain. Steps were taken to reduce or eliminate dynamic mesh refinement based on curvature or other geometric details so that all controllable mesh parameters become a function of base mesh size.

STAR-CCM+ Design Manager was utilized to perform two parametric sweeps using the same domain. The sweeps varied the fluid, the shell, and the surface wrap mesh base sizes between 0.001 and 0.01 m, with step sizes of 0.00225, leading to 125 designs per parametric study. The first sweep was performed utilizing STAR-CCM+ interface contacts, and the second sweep was performed utilizing the Data Mappers tool, leading to 250 unique simulation results. Hence forth, mesh size for the remainder of this section specifically refers to the Mesh Base Size.

Contrasting figures 3.12 (a) and (b), it can be seen that a generated interface misses a substantial potion of either or both surfaces, with the interface in figure 3.12 (b) capturing only 64 percent of the solid surface elements. From this comparison, the need for investigating the influence of mesh parameters on the quality of the interface becomes clear.

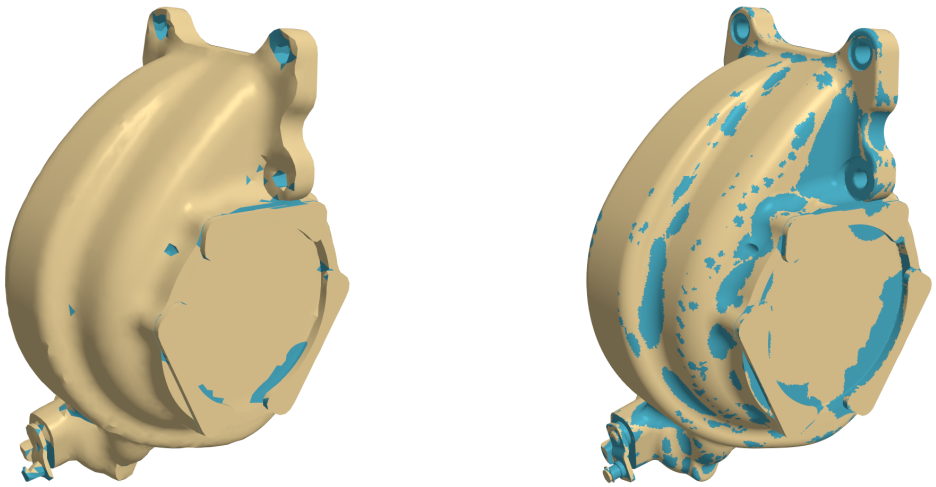

(a) (b)

Figure 3.12: (a) Image of the primary turbine of the turbo compound with interfaced elements in yellow and non-interfaced elements in blue. Meshes are uniform at 5mm base size each. (b) Meshes are non-uniform at base sizes of 3.25mm in the fluid fluid, 1mm for shell, and 10mm for the surface wrap

Three main responses from the this parametric study were analyzed. The first response is unmapped solid elements. This is represented as a percentage of the solid surface mesh elements that are not included in the interface communication. The second response is unmapped fluid elements. Similar to unmapped solids, this represents the percentage of surface or face elements of the fluid mesh that are not captured in the interface. For both these responses, the ideal value would be zero unmapped elements indicating a perfect interface. The third response is the heat flux measured through the interface between the solid and fluid continua.

Figures 3.13 and 3.14 below are parallel plots showing the respective response of unmapped solid element percentage and unmapped fluid element percentage. These plots show the 25 best and 25 worst trials to highlight the trends. Connected lines on the parallel plot represent a single trial. The first three bars from left to right represent the input trial parameters. The fourth bar represents the corresponding response given the first three input parameters. As an example, one trail can be seen with input parameters of a fluid mesh base size of 10 mm, a shell mesh base size of 10 mm, of 3.25 mm. These inputs then corresponds to an unmapped solid element response of approximately 3 percent. This example can be seen through the black dashed line.

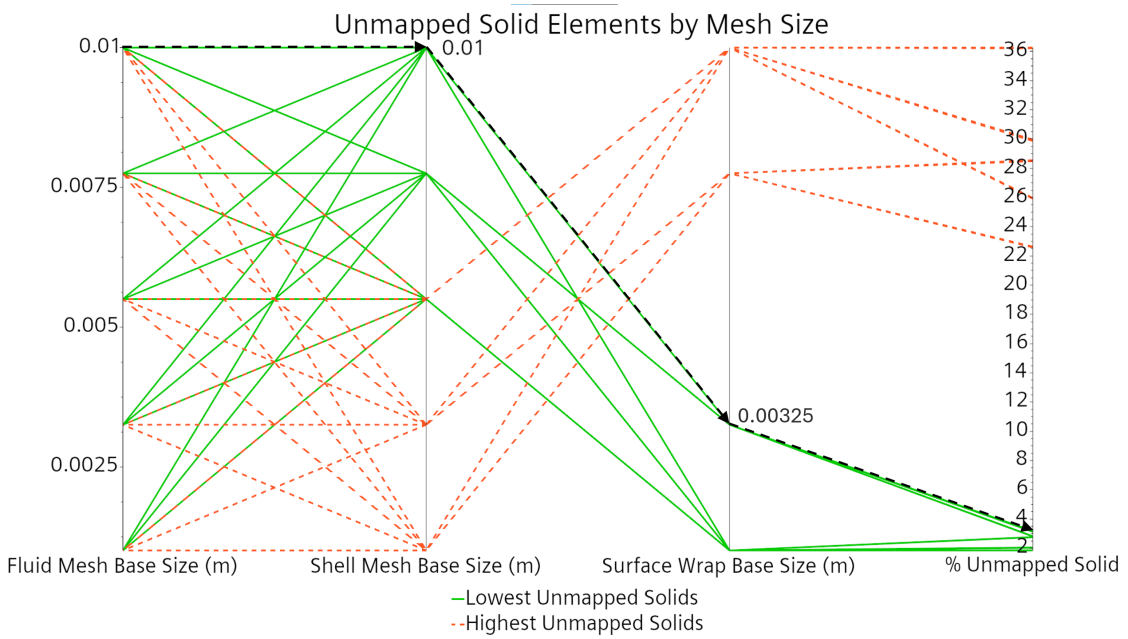

Figure 3.13: Unmapped Solid Elements Parallel Plot. Example from text in black dashed line.

From figure 3.13, several observations can be made. The first is that the unmapped solid elements seems to be independent from fluid mesh size. This will also be seen to be the case for unmapped fluids. This suggests that the input surface used to generate the fluid mesh dictates the interface to the fluid mesh. Due to this, for the remainder of this section, data will be shown for only one fluid mesh base size unless otherwise notably of interest as the data typically remains consist for each

fluid mesh base size parameter. The second observation is that the best trials occur when the base size for the surface wrap operation is at most half that of the solid or shell mesh. The opposite is then also observable, as the worst performing trails for unmapped solid elements are those where the surface wrap size exceeds the shell mesh.

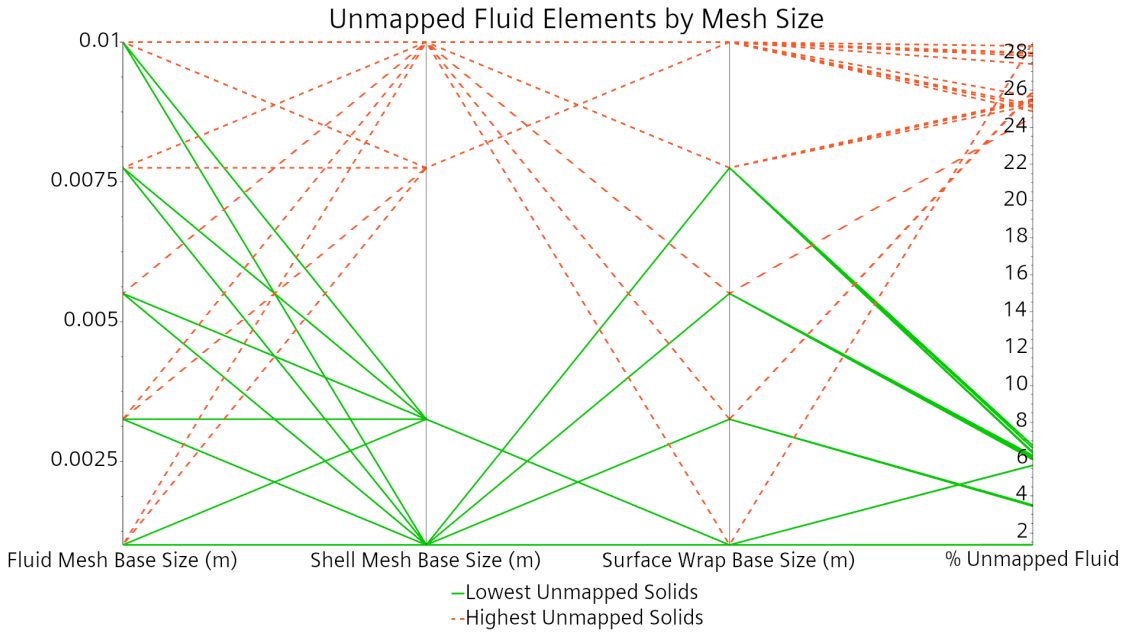

Figure 3.14: Unmapped Fluid Elements Parallel Plot

Figure 3.15 below shows the relationship between the solid's shell mesh and the surface wrap base sizes. With the red line depicting the difference between the surface wrap and the shell mesh sizes, it is observed that the lowest unmapped elements results from a surface wrap that is up to half as fine as the shell mesh.

The consequence of an imperfect interface is that the communicating surface area between meshes are reduced. In this study, as a constant heat source is applied on the inner surface of the turbo, the flux seen through the interface can be analyzed to understand the interacting behavior. Figures 3.16 (a) and (b) show the relationship between unmapped fluid and solid unmapped elements versus the resulting flux seen through the interface normalized against the expected boundary heat flux. The output heat flux was normalized by the input heat flux through the specified heat source. It can be observed that unmapped fluid interface elements have no correlation to variations in flux through the interface. Unmapped solids, however, appear to be directly correlated, suggesting a near linear relationship between an increase in unmapped elements and an increase in boundary heat flux.

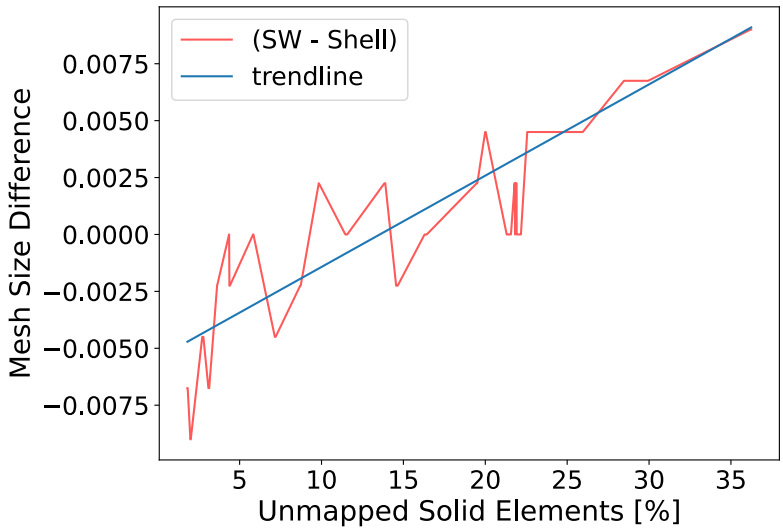

Figure 3.15: The difference in mesh size plotted against unmapped solid elements. SW - Shell is to indicate the shell mesh base size is subtracted from the surface wrap base size

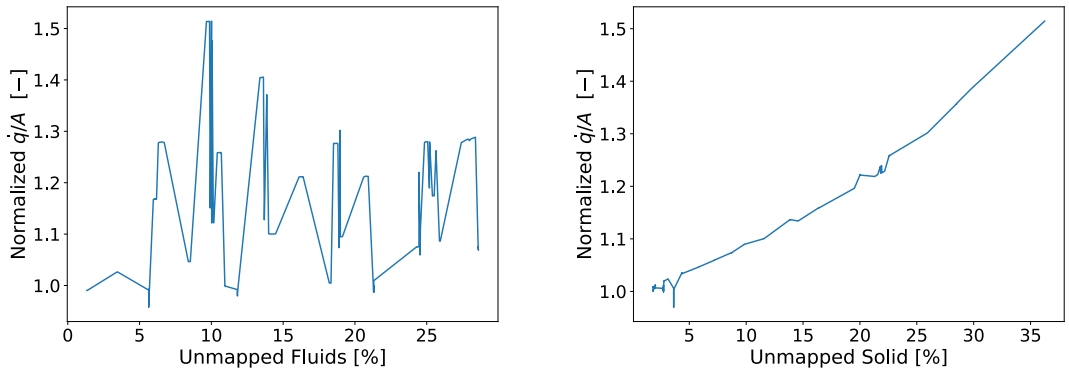

(a) (b)

Figure 3.16: (a) Boundary heat flux through the interface normalized against the expected boundary heat flux versus unmapped fluid elements; no correlation is evident, (b) Normalized heat versus unmapped solid elements. Direct correlation is evident

This correlation is made more clear in figure 3.17 (a) and (b) below, showing a contour of the normalized heat flux through the interface compared to a contour of unmapped surface elements. It can observed that these contours follow very similar behavior, indicating a direct correlation.

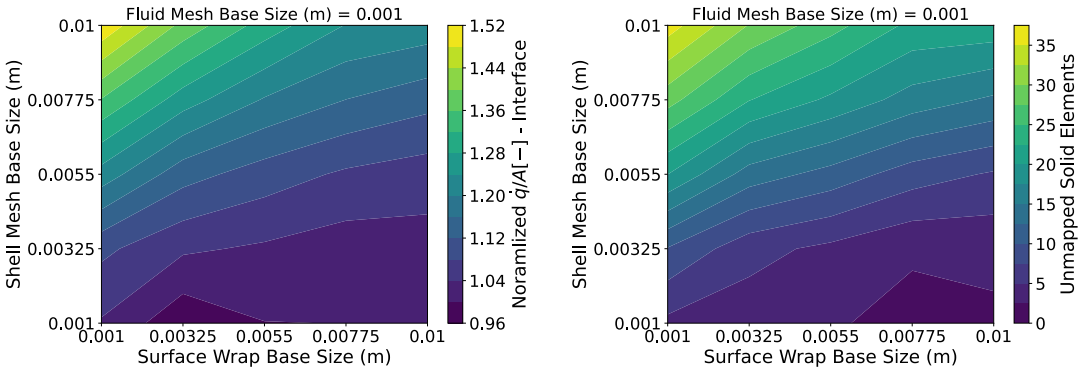

(a) (b)

Figure 3.17: (a): contour showing flux through the available interface area for varying shell mesh and surface wrap base sizes, (b) contour showing unmapped elements for varying shell mesh and surface wrap base sizes

Figure 3.18 below contour of normalized heat flux as a function of base size of the surface wrap operation and shell mesh. Here the data mapper approach is used instead of using interfaces obtained from surface contacts. It can be observed that the flux communicated through data mappers is essentially freed from reliance on a high quality interface or high quality mapped facet area. This is because data mappers uses all the surface vertex data to interpolate to the communicated mesh rather than relying on specific cell-to-cell communication. As seen below, this leads to a much more consistent flux for varying mesh sizes. This small variation is due to the small changes in surface area resulting from differing meshing conditions. As can be seen, the error introduced through interpolation is no more than ~2 % for the course meshing conditions. The normalized heat flux approaches a value of 1, representing near zero error, for high quality meshes.

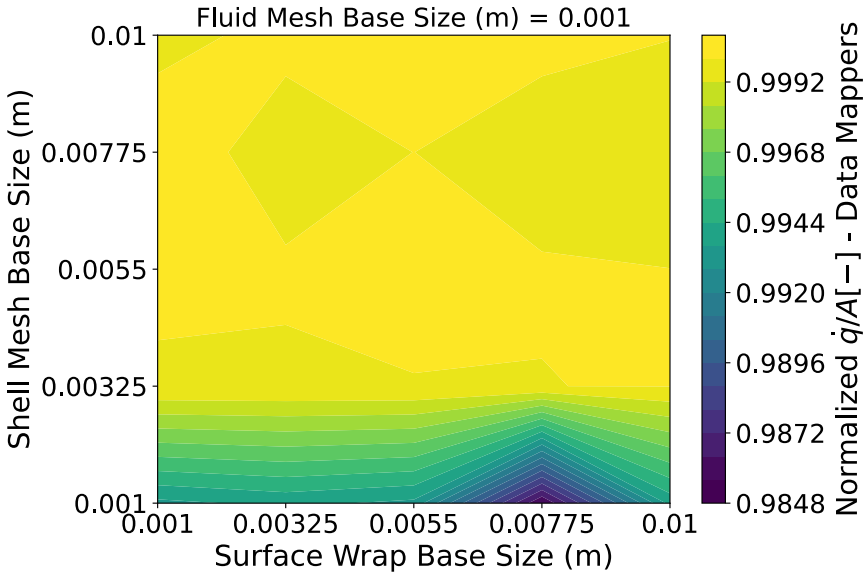

Figure 3.18: Contour plot showing the resulting heat flux through the interfacing surface for data mappers communication

The study explored in this section has examined the interfaces through STAR-CCM+'s interface pipeline as well as using data mappers which directly interpolates the data instead. It has been demonstrated that, while it is possible to achieve a contact interface that does not impact the resulting flux, particular care must be taken to ensure that the interface accurately and uniformly captures the expected physical behavior of heat transfer through the contacting surfaces. This could be too cumbersome to be implemented for a full-scale model considering a very large number of interfacing surfaces. Alternatively, data mappers served as an accurate baseline for expected flux. While familiar trends can be observed, i.e. when the shell mesh is too course, regardless of the matching surface wrap, the resulting flux through the generated interface increases proportionally to the number of unmapped solid elements, the resulting flux still remains much closer to an expected value. As such, the method adopted the use of data mappers to communicate the mesh continua instead of the STAR-CCM+ contacts interfacing pipeline.

3.4 Boundary and Material Conditions

The three main different types of boundary conditions specified in this CHT simulation are velocity inlet at the inlet of the climatic chamber, pressure outlet at the chamber outlet and constant temperature and convection at surfaces of the heat source boundaries. Boundary condition on the walls of the domain are set as a no-slip wall. The boundaries of components that are considered in the conjugate heat transfer study take the mapped temperature boundary condition, which is updated at the end of each loop using the values of temperature obtained from solid and shell continua.

The boundaries present within the solid and shell continua are assigned either explicitly specified or mapped boundary conditions. Mapped boundary conditions establishes data mapping from the fluid continuum to the solid continuum and vice-versa in a CHT simulation. The values of these boundaries were established using a mix of historical test data and results of other component-level simulations. Boundaries which are strongly affected by different modes of heat transfer and which experience temperature gradient at different operating conditions are given through mapped convective boundary condition.

Components having materials that followed a multi-layered structure were modeled as shells to take advantage of STAR-CCM+ workflow with these models. The material properties for all components were selected using Volvo's internal database. Components expected to experience high temperature used material models with thermal conductivity and specific heat as a function of temperature.

3.5 Steady-state Simulations

Using the aforementioned models and boundary conditions, a steady state simulation model built for CHT simulations. Four different engine operating points are simulated using the steady-state model. Inputs to the simulation models are provided based on the test data provided. These inputs include different parameters such as fan speed, coolant flow to the radiator, heat rejected by the radiator, air flow to the CAC and temperature at CAC outlet. The relative difference of these parameters in the operating conditions 2, 3, and 4 with respect to operating condition 1 are shown in table 3.1.

Table 3.1: Summary of the input parameters to simulate four different engine loading conditions.

	Op1	Op2	Op3	Op4
Fan Speed	v_f	$1.24v_f$	$1.39v_f$	$1.65v_f$
Coolant Flow	$\dot{m}_c$	$1.26\dot{m}_c$	$1.42\dot{m}_c$	$1.67\dot{m}_c$
Rad Power	P_{rad}	$1.32P_{rad}$	$1.42P_{rad}$	$1.46P_{rad}$
CAC Flow	$\dot{m}_{cac}$	$1.21\dot{m}_{cac}$	$1.29\dot{m}_{cac}$	$1.37\dot{m}_{cac}$
CAC Temp	T_{cac}	$1.09T_{cac}$	$1.09T_{cac}$	$1.06T_{cac}$

Limited data of measured component temperature are available for the four different operating conditions from the tests. The full scale under-hood simulation was performed at these four differing engine loading cases in order to compare simulated data to the available experimental data.

4
Results

Results from the simulations are presented in two sections. The first section presents results from steady-state simulations compared with available test data. The second section presents the results from various parametric studies. These studies serve to expand the robustness of the methodology by providing additional insight into different simulation parameters.

4.1 Steady-state Model

This section presents results obtained from a steady-state simulation of the vehicle under-hood for the four different engine operating conditions described in section 3.5.

Figure 4.1 below depicts the engine block and the surrounding components on both the Left Hand Side (LHS) and Right Hand Side (RHS) of the engine. The component surface temperatures serve as a good indicator of the local under-hood temperatures. The difference in surface contours relative to engine loading operation condition is relatively small.

It can be seen that the LHS is substantially cooler than the RHS. The temperature on the LHS is largely dictated by the air temperature from the cooling package. This is due to the absence of major heat sources on the LHS. Lower temperatures can be observed towards the bottom of the under-hood region. This is because the radiative influence of the hot exhaust system becomes negligible in the underside of the under-hood, and cool air from under the grill is able to enter and provide additional cooling.

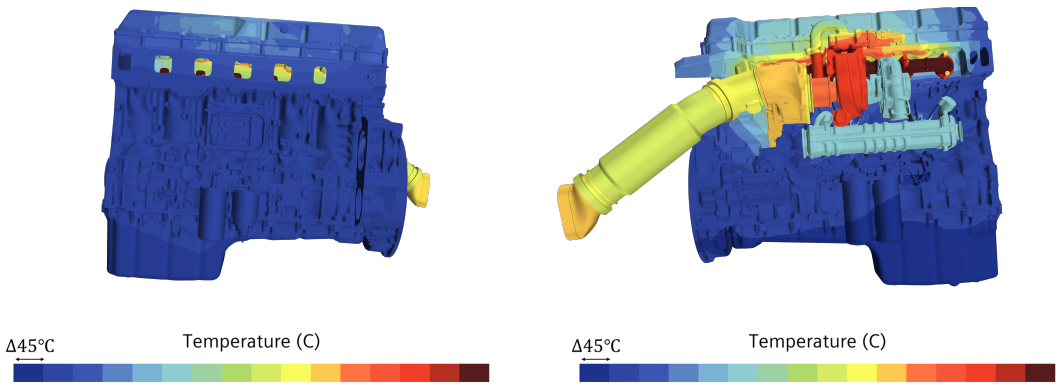

(a) LHS (b) RHS

Figure 4.1: Temperature Contour of the Engine and attached components - representative of the LHS and RHS under-hood temperatures at Loading Conditions 1 (Op1)

The RHS of the under-hood is a radiation-dominant region. The surfaces temperatures of this region are largely dictated by the exhaust gases from powertrain components. The heat source from the exhaust gas is specified as a boundary condition using a combination of constant temperature and convective boundary conditions on the surfaces of components that are in direct contact with the exhaust gas. It follows that the hottest components are those interacting with the exhaust gas more quickly after combustion - the exhaust manifold shows the highest temperature, with the turbocharger turbine and EGR valve showing a lower temperature, and the decrease in temperature continues until the end of the exhaust line into the EATS system (not shown). The convective exchange with the air exiting the cooling system also creates a visible temperature gradient across the exhaust system components. The convective energy exchange heats the rear of the engine assembly and under-hood compartment.

Figure 4.2 shows a filtered part selection that act as the only source of boundary irradiation for the following filtered incoming radiation contours and other plots. This is done to explicitly analyze the specific contribution of radiation from the exhaust assembly incident on the noise shields. This is shown in figure 4.3.

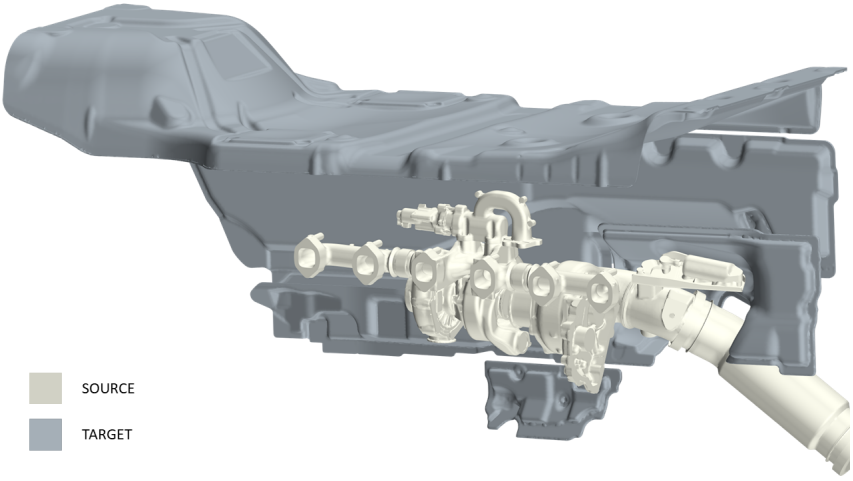

Figure 4.2: Components involved in radiation exchange. Primary radiation sources (exhaust assembly) shown in ivory and sinks (noise shields) shown in gray.

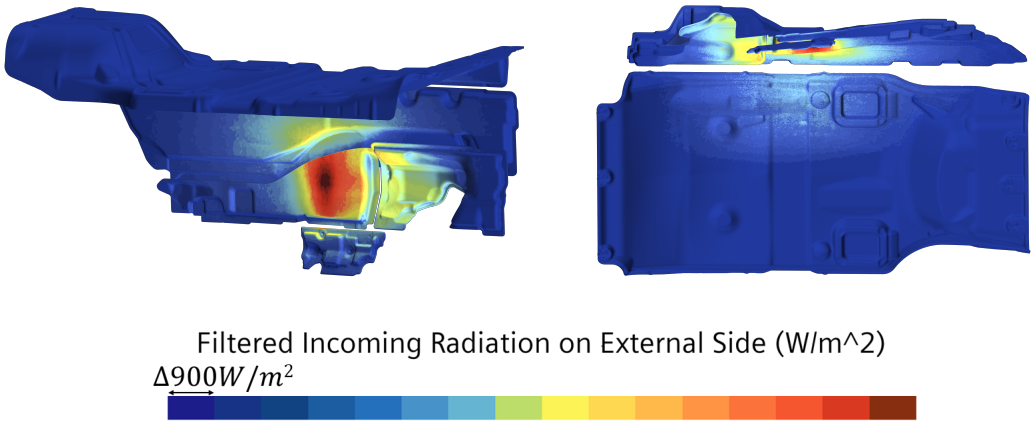

Figure 4.3: Incident radiation on the noise shield considering only the components in the exhaust assembly as heat sources

Figure 4.4 compares the irradiation on the Air Valve Unit (AVU), Valve Cover (VC), Noise Shield (NS), Exhaust Gas Recirculation Heat Shield (EGR HS), Closed Loop Butterfly valve (CLB), and the Valve Frame (VF) from the exhaust system. These components are showin in section 3.1.1 from figure 3.1 to 3.5. The values of the incoming radiation closely follows proximity to the exhaust system as well as direct line-of-sight, translating to high view factors (see section 2.2.4). There is an observable variation in boundary heat flux values between the different engine operating conditions for some components. This is due to variations in surface temperatures resulting from different convective conditions for each simulated engine operating condition. The variation in the convective conditions are due to the changes in vehicle and fan speed for the different engine operating conditions. It can be observed that the flux variations are not necessarily linear with increased convection from fan

speed, or under-hood air bulk velocity, stemming from complexity of the different heat transfer modes between the under-hood components. This is most obvious with the heat flux record on the VF. The AVU does not have any values for incoming radiation due to having 0 view factors from the source components shown in figure 4.2 filtered components.

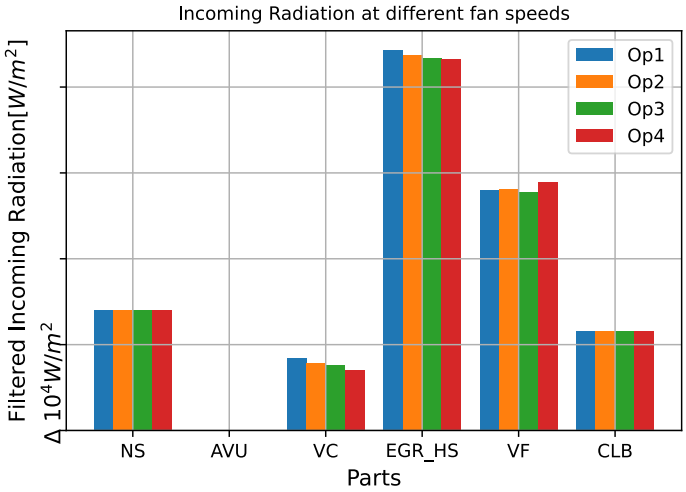

Figure 4.4: Incoming radiation for the four operating Conditions.

Figure 4.5 shows the maximum boundary heat flux on the various component surfaces. This boundary heat flux includes all forms of heat transfer, whereas figure 4.4 compares only irradation. The values for the valve cover, the noise shield, and the EGR heat shield all have lower boundary flux values than incoming radiation flux for each operating condition. This is a consequence of high convective heat transfer between the components and the surrounding air, which is at a lower temperature. This is especially noticeable for the EGR heat shield, which receives more than 40,000 W/m^2 through irradation but has a maximum boundary heat flux of below 2,500 W/m^2. The AVU and CLB, however, have higher maximum boundary flux values than incoming radiation flux. This indicates that these components are receiving additional energy from conduction and/or convection.

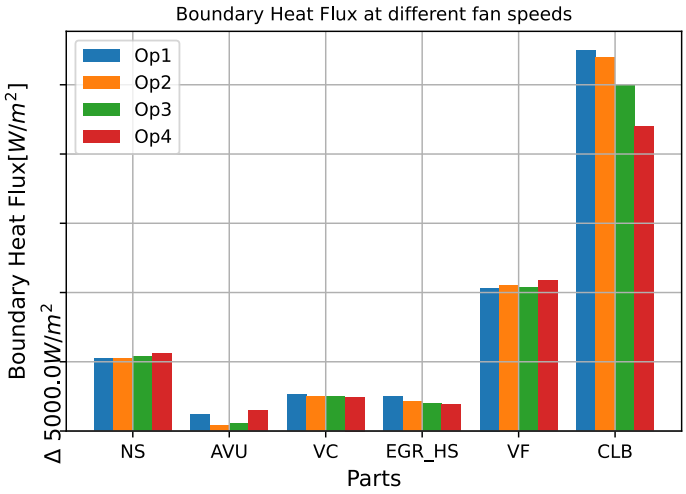

Figure 4.5: Maximum boundary heat flux at the four operating conditions

Figures 4.6 and 4.7 show the average surface temperatures and the maximum temperature respectively of the selected components at the varying engine operating conditions. From these figures it can be seen that, the average temperature for engine operating condition 2 ($Op2$) is slightly higher than for operating condition 1 ($Op1$). This is mainly due to the non-linear relation between the heat rejected by the cooling package and the increasing fan speed. While the fan speed is increasing from Op1 through Op4, the temperature also increases in certain cases because more heat is rejected from the cooling package in these cases.

Both these plots show similar trends with respect to decreasing surface temperatures from Op1 to Op4. This indicates that the increase in convective cooling from the increase in fan speed displaces more energy than is supplied to the system through the additional cooling package heat rejection. For either plot, the highest temperature components are those in closest proximity, have high view factors, or both, to the exhaust assembly components.

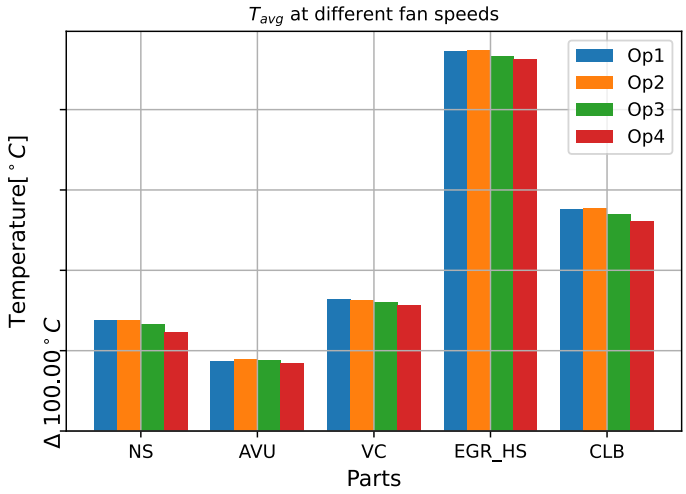

Figure 4.6: Average surface temperature through the four operating conditions

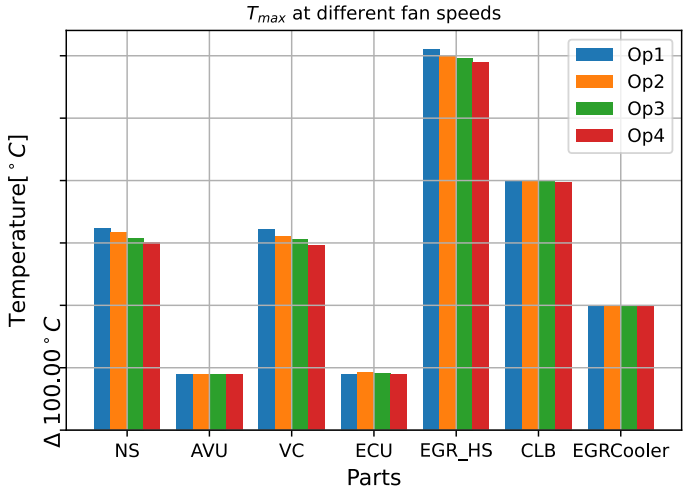

Figure 4.7: Maximum surface temperature through the four operating conditions

The results from the simulation are compared with the tests carried out at the climatic wind tunnel. These tests were carried out for the same four steady state engine operating conditions and the temperatures were measured on various components. Components for comparison were chosen such that the location of one of them is radiation dominant and the other is located in the convective region, without any dominant source of radiation in its vicinity. CLB located on the RHS is in a radiation dominant region while AVU located on the LHS is in a convection dominant region. The location of probes to capture the surface temperature is similar to that of location of surface-mounted temperature sensors used in the test. Figures 4.8 (a) through (d) compare the temperature data gathered from the aforementioned probe locations within the under-hood. The probe identifications have been changed to

component name followed by P1 and P2 to refer to probe 1 and probe 2 for the specific component.

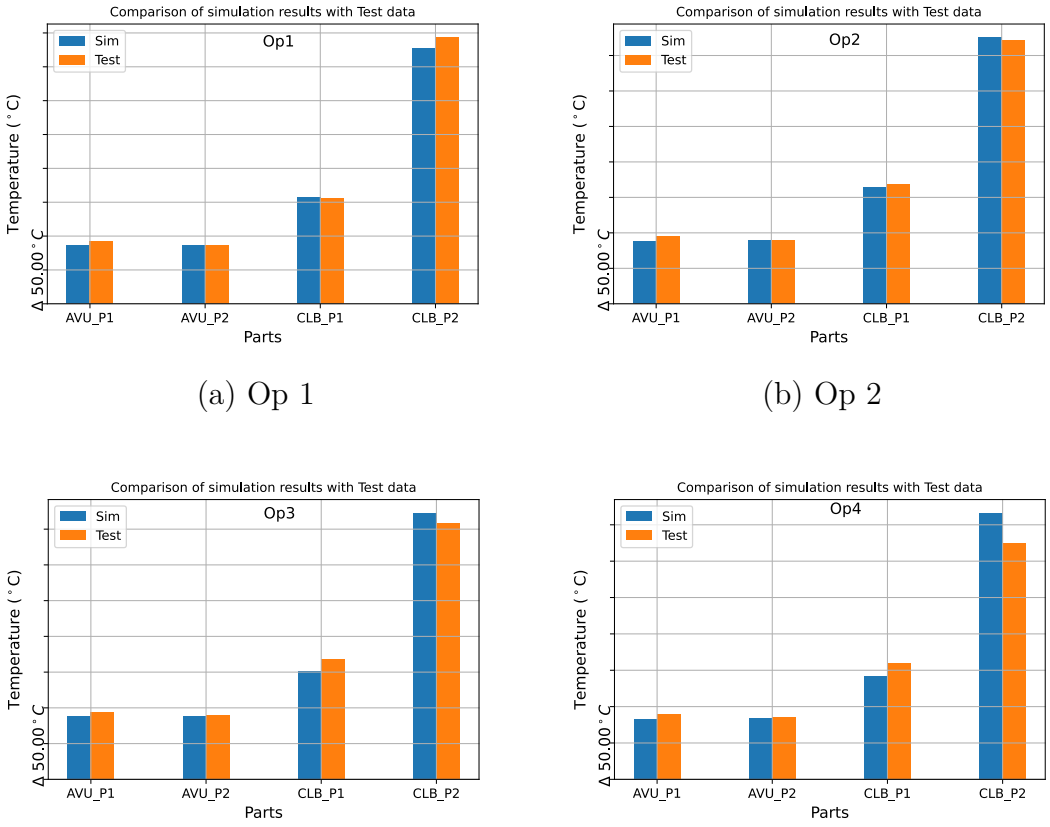

(a) Op 1

(b) Op 2

(c) Op 3

(d) Op 4

Figure 4.8: Comparison of simulation and test data for the different operating conditions

The comparisons show reasonable agreement for the air valve unit and close-loop butterfly value probe locations, with Op4 showing the highest difference.

4.2 Parametric Studies

As a robust commercial CFD software, STAR-CCM+ offers customization of a large number of simulation parameters that can have large effects on simulation results. Four different parameter were selected to be studied in detail to better understand the impact that they may have on the simulation. These studies include first looking at the looping frequency of the continua solvers, then the impact of differing RANS turbulence models, followed by the impact of cell shape, and lastly the influence of radiation patch-face proportion.

4.2.1 Sensitivity to CHT Looping Frequency

The solved values of state variables in different physics continua need to be communicated, i.e., the temperature from solving conduction and radiation in the solid and shell continua is mapped to fluid continua. Similarly the calculated values of heat transfer coefficient and local reference temperature from the fluid continua are mapped to the solid continua. The mapped values of these variables from each continua are updated as boundary conditions for the other continua during the simulation. One complete mapping cycle consists of mapping temperature from solid and shell continua to fluid continua and mapping of heat transfer coefficient and local reference temperature from fluid continua to solid and shell continua form one loop of mapping of data. Four simulations were performed for different looping frequencies to observe and study the effect it has on various parameters such as values of results, stability and simulation time. The mapping frequency was varied while keeping the stopping criteria, maximum iterations limit and the solver setting unchanged. In study 1, the loop frequency was set to one, which implies the mapping of data between the continua happens after every iteration of the simulation. In study 2, study 3 and study 4 the calculated state variables were mapped after every 50 iterations, 100 and 200 iterations, respectively. All the four studies were performed for operating condition 1 to 4 and same set of boundary conditions.

Reports of maximum temperature, average temperature, boundary heat flux and filtered incoming radiation are recorded for a set of components. Along with the temperature reports, total solver elapsed time is monitored for all four studies. Parts that are radiation-dominant and parts that are convection-dominant are monitored. The average and maximum temperatures on these parts are compared for different looping frequencies and plotted as shown in the figure 4.9 and 4.10. From these plots it can be seen that changing the frequency of mapping does not significantly affect the values of temperature.

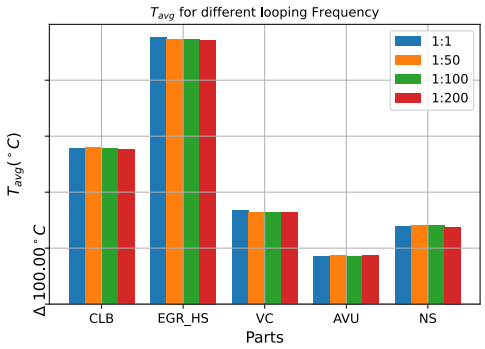

Figure 4.9: Average Temperature

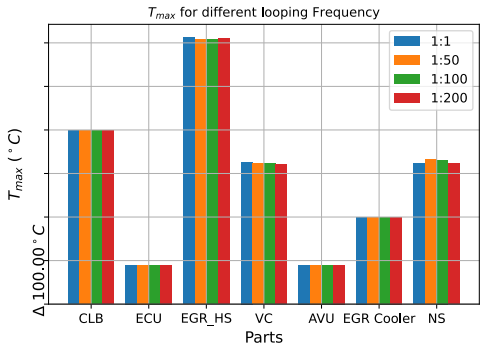

Figure 4.10: Maximum Temperature

Comparison of solver elapsed time is shown in figure 4.11. The higher the number of looping count, the more time the solver takes to reach the stopping criteria. This is because the exchange of information and updating of values of the state variable takes time. Since there is no significant effect on the surface temperatures, incoming

radiations and boundary heat flux it is better to set a higher looping frequency to achieve a lower solver elapsed time.

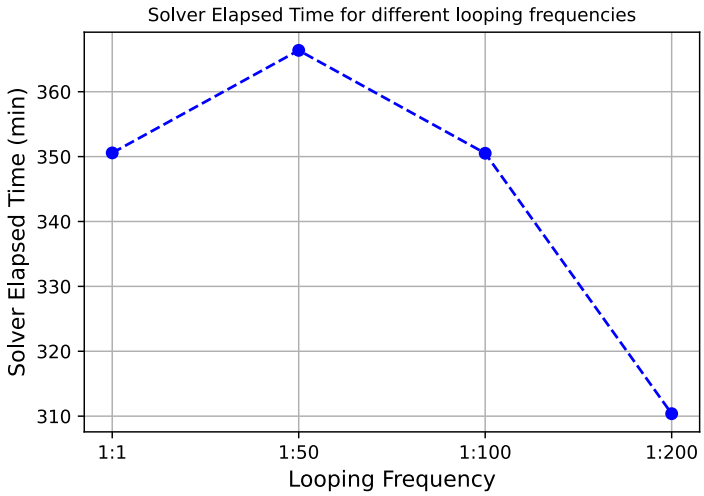

Figure 4.11: Solver Elapsed Time for different Looping Frequencies

Table 4.1 shows the number of loops completed by each study along with the solver elapsed time. The four studies were simulated using 640 cores on the same HPC cluster. It can be observed that the solver elapse time for 1:1 does not follow the trend seen in the other trials as it completes faster than 1:50. Further investigation is required to explain this behavior.

Table 4.1: Study summary

	Looping Frequency	Number of Loops	Solver elapsed time (min)
Study - 1	1:1	7500	350.57
Study - 2	1:50	150	360.37
Study - 3	1:100	75	350.51
Study - 4	1:200	37.5	310.31

4.2.2 Sensitivity to Turbulence Modeling

This study investigates the effect of choice of turbulence modeling resulting surface temperature. Two simulations with polyhedral mesh, looping frequency of $1:200$, and a stopping criteria of maximum steps of 15000 was executed. One simulation used a $k-\epsilon$ turbulence model, while the other used a $k-\omega$ SST turbulence model. The motivation behind choosing these models for study is the ability of handling the separated flow by $k-\epsilon$ and the ability to capture the near wall behavior by $k-\omega$ without use of any damping functions. Average and maximum surface temperatures

are monitored. Comparison of the same for different components are shown in figures 4.12 and 4.13.

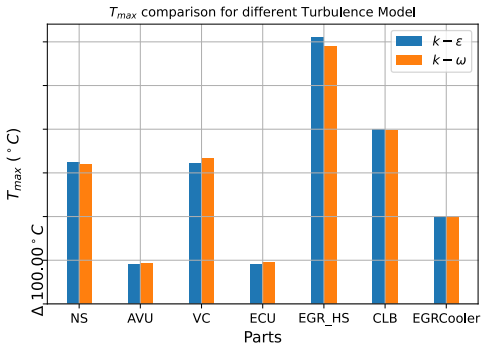

Figure 4.12: Comparison of T_{max} for different Turbulence Models

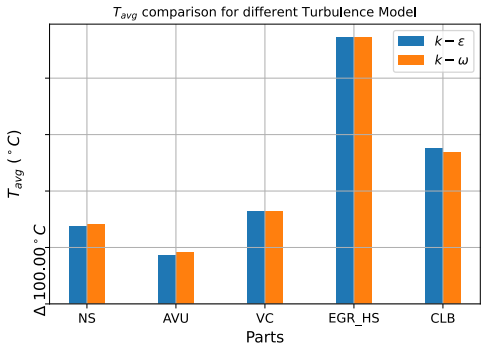

Figure 4.13: Comparison of T_{avg} for different Turbulence Models

From figure 4.12, a slight difference in the maximum temperature value for the Valve Cover (VC), EGR heat shield (EGR_HS), and Noise Shield can be observed. However, on comparing the values of average temperature, almost no difference in values were observed. This implies that the selected turbulence model may influence hot spot temperature resolution of the model, but does not meaningfully impact average temperatures.

The results of the turbulence models are compared to the available test data below in Figure 4.14. The probe locations within the models, located to reflect physical probe locations during testing, were kept identifical for both turbulence models. The probe was unable to return data for the AVU probe 2 for the $k-\omega$ simulation, however. The reason for this is unknown and requires further investigate.

From this comparison, it is observable that the the $k-\epsilon$ model more closely aligns with the limited test data. This implies that STAR-CCM+'s $k-\epsilon$ model is likely sufficient for large-scale models. In order to draw any definitive conclusion pertaining to which model yields more accurate result, however, tailored validation testing would need to be performed to eliminate any testing uncertainties and then compared against purpose built simulation model.

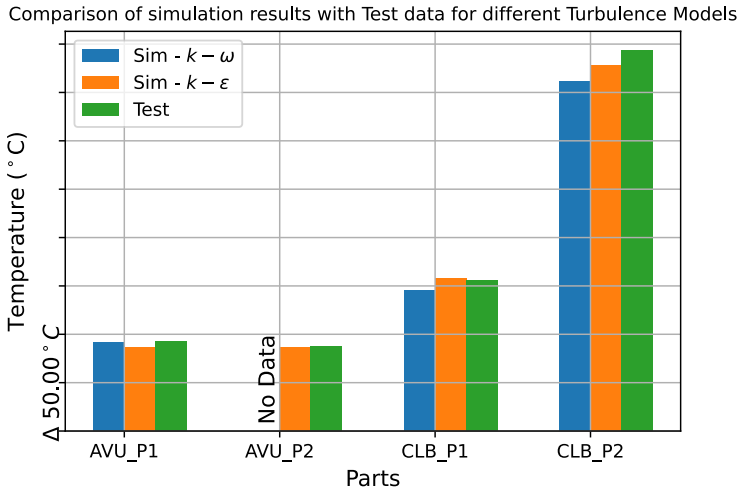

Figure 4.14: Comparison of simulation and test data for different Turbulence Models

4.2.3 Sensitivity to Cell Shape

A simple study was performed to understand the potential impact of different cell shapes on the scalar fields of interest within a CHT simulation, primarily temperature. Two studies were performed using a polyhedral and trimmed cell (i.e.hexaheral) mesher respectively. All meshing parameters were kept the same. The simulations were executed at the same engine operating conditions and for the same stopping criteria of a set 15000 iterations. Reports of maximum and average temperatures were generated for selective components along with solver elapsed time.

Table 4.2: Cell and face count for polyhedral and trimmed mesher

	Polyhedral	Hexahedral
Cell Count	99 656 350	97 136 776
Face Count	470 407 434	304 461 511

Table 4.2 shows the number of cells and faces in the entire domain for polyhedral and trimmed hexahedral mesher. The high face count of polyhedral mesher is due to the fact that average number of faces per cell is 14 [17]. On the other hand number of faces a hexahedral mesh can have for each cell is always six. Front section view of the under-hood region for polyhedral mesher and trimmed hexahedral mesher are shown in figures 4.15 and 4.16.

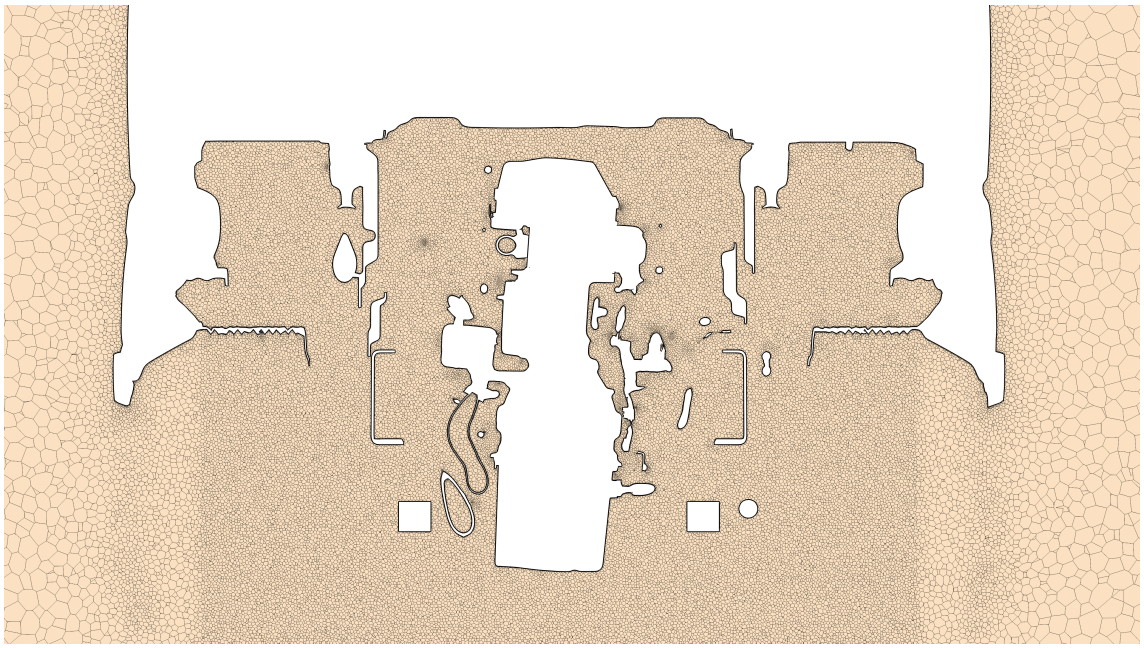

Figure 4.15: Planar section view of under-hood region with polyhedral mesh

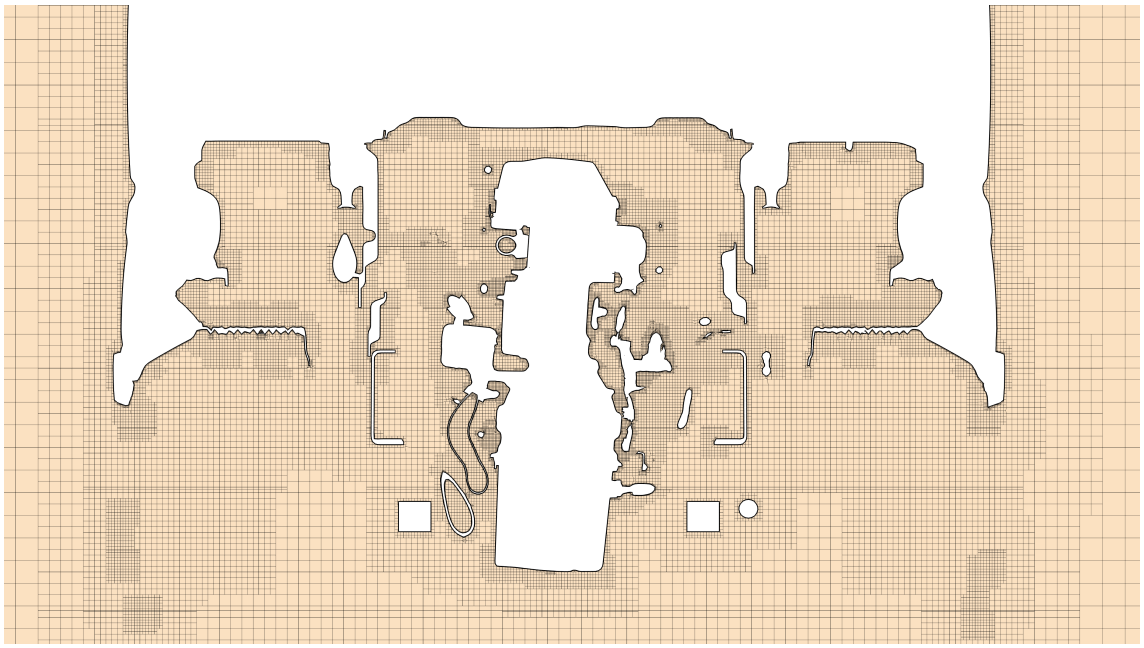

Figure 4.16: Planar section view of under-hood region with hexahedral mesher

Comparison of maximum and average surface temperatures on the components are shown in figure 4.17 and 4.18. From these plots it can be seen that there is a slight difference in the values of temperature between the two types of mesher. However, it can be seen that the values are slightly lower in case of trimmed hexahedral mesher than the polyhedral mesher. Seeing no significant differences in temperature, solver

elapsed time was monitored. Table 4.3 shows the time taken by the solver to reach the similar stopping criteria with different meshers. With almost two million cells less than the polyhedral mesher, hexahedral mesher takes 248 minutes more to run the same number of iterations than the polyhedral mesher. One of the conjunctures for the increased solver time may be due to the increased number of inner iterations that the solver needs to run to meet the numerical convergence of the segregated flow solver. The advantage of using a polyhedral mesher over hexahedral is the high number of cell faces which can handle and resolve regions with high turbulent much better than the hexahedral mesher. The additional faces in a polyhedral mesh captures transported variables between the cells in more orthogonal directions than that in a hexahedral mesh, thus resulting in lower numerical errors and reducing numerical diffusion.

Table 4.3: Solver elapsed time for polyhedral and hexahedral meshes

	Polyhedral	Hexahedral
Time (min)	310	558

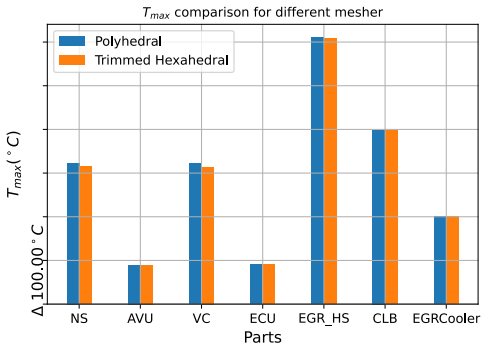

Figure 4.17: Comparison of T_{max} for polyhedral and hexahedral mesher

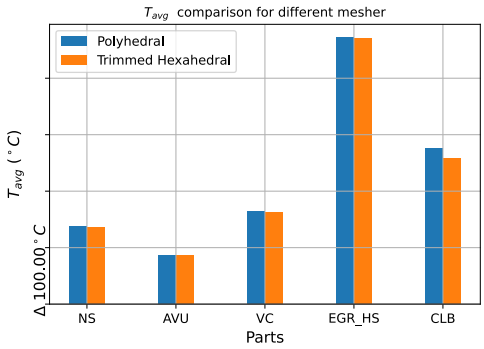

Figure 4.18: Comparison of T_{avg} for polyhedral and hexahedral mesher

4.2.4 Sensitivity to Radiation Patch-Face Proportion

Surface radiation is numerically solved by initially dividing the surface into multiple small segments using the spatial discretization known as patches. The view factors are then calculated by ray tracing. The view factor count is quadratically proportional to the number of patches. Consider for example there are 2 million patches, then the number of view factors traced by the solver will be 4×10^{12}. This process is computationally expensive due to time and memory required to calculate these view factors. Considering each view factor utilizes 8 bytes of memory then in order to calculate 4×10^{12} view factors, 32×10^{12} bytes of memory i.e 32 terabytes of memory is needed. It it thus obvious that the number of patches in the radiation model has an effect on the memory and cost of the simulation. Thus it is important to decide

the number of patches needed and how the temperature changes when changing the number of patches.

In order to understand the balance of radiation resolving fidelity versus cost, a parametric study was performed to observe the changes in component temperature for varying amounts of patches. The amount of patches is controlled through the parameter Patch-Face proportion, which as a percentage determines the number of faces included within a single patch. A patch-face proportion of 100 % indicates that each surface face is treated as a radiation patch, while a patch-face proportion of 1 % indicates that 99 % of the surface faces are lumped into a single patch. Components are grouped as sources and targets based on their respective roles in the radiation exchange. The components and their grouping are shown in the figure 4.19.

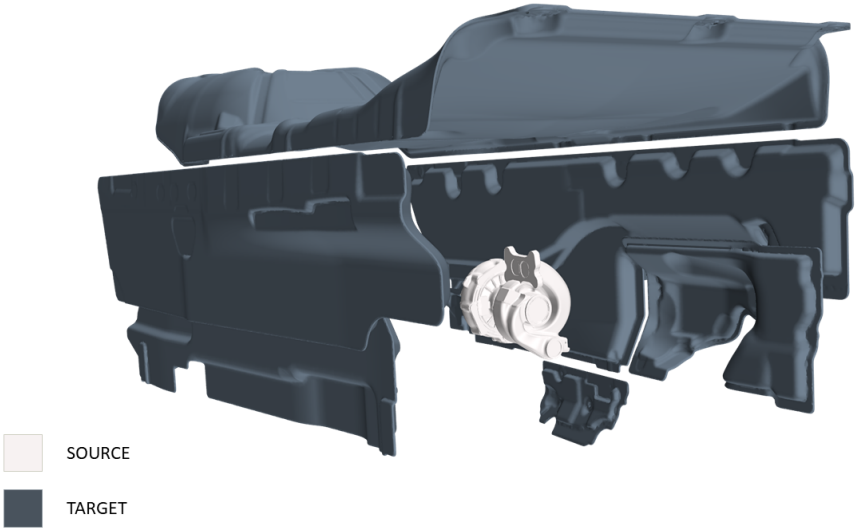

Figure 4.19: Grouping of source and target for parametric sweep study

The parametric sweep is divided into two studies where in both studies the patch-face proportion on the surfaces of the source is kept constant at 50 and 25 in Study 1 and Study 2 respectively. For these values of patch-face proportion on the source, the values of patch-face proportion on the target is swept across four different values of 50, 30, 25 and 10. The default value of patch-face proportion is 100. Table 4.4 shows a summary of the studies performed. Consider Study-1, 50-50, 50-30, 50-25 and 50-10 are four cases studied. In each of these cases, the first number indicates the patch-face proportion used for the source components, and the second number indicates the patch-face proportion used for the sink components.

Table 4.4: Breakdown of radiation patch-face proposition parameters compared

	1	2	3	4
Study 1	50-50	50-30	50-25	50-10
Study 2	25-50	25-30	25-25	25-10

Figures 4.20 through 4.23 below show the maximum and average surface temperatures on the noise shield and CLB, respectively. From figure 4.20, it can be observed that the noise shield maximum temperature change is primarily dependent on the patch-face proportion of the sink components as both source values of 50 and 25 depict similar trends. The average temperature of the noise shield, however, is generally unaffected by varying either the source or sink patch-face proportion as seen in figure 4.21.

From figure 4.20 it can be seen that the trend for both the studies are similar. The temperature difference for studies with different patch-face proportion on the sink is significant. It was observed that with reducing the patch-face proportion on the sink, the value of the calculated temperature reduces. However, this trend is not the same for all components. Figure 4.22 shows the variation of maximum surface temperature on the CLB for different patch-face proportions and it can be seen that changing the value of patch-face proportion on the sinks does not significantly affect the change in surface temperature of CLB. In order to understand the effect of change in patch-face proportions on surface temperature, average temperature on these surfaces were recorded. Figures 4.21 and 4.23 shows the average temperature on Noise shield and CLB respectively. It can be seen that there is no significant change in the average temperature on the surface of Noise Shield. However, a significant change can be seen on the surface temperature of CLB.
From these figures, it may be concluded that the value of patch-face proportion on the sinks affect the temperature distribution significantly rather than the patch-face proportion value on the source. The other possible reasons for noticing anomaly in the temperature trends between the components is due to the dependency of patch-face proportion with respect to the shape and spatial orientation of the components.

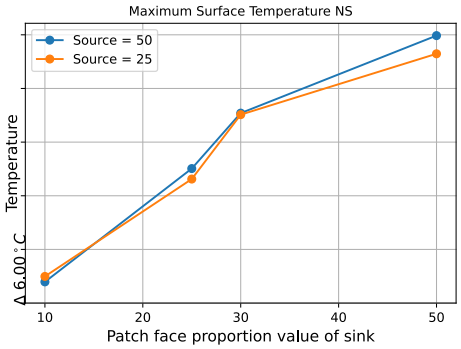

Figure 4.20: Maximum Temperature - Noise Shield

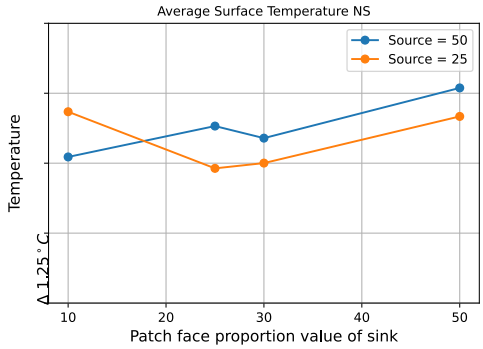

Figure 4.21: Average Temperature - Noise Shield

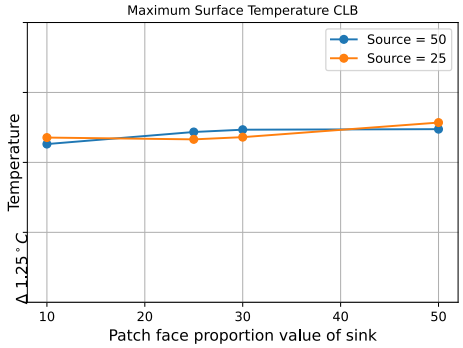

Figure 4.22: Maximum Temperature - CLB

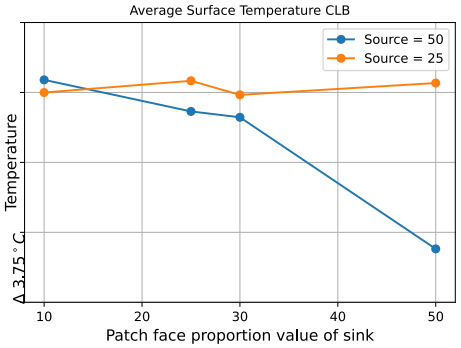

Figure 4.23: Average Temperature - CLB

5
Conclusion

The following conclusions are drawn towards the stated objectives of this work.

STAR-CCM+ provides a viable platform in which a full-scale under-hood CHT simulation may be performed in a single model and single file. Additionally, the limited available test data corroborates with the results from the developed steady-state methodology utilizing data mappers.

Interfaces are highly mesh-dependent and can affect the heat transfer between meshes if poorly resolved. This can cause unphysical hot spots. This behavior requires further study to fully comprehend to what extent it may affect simulation results. Conversely, data mappers are useful in connecting meshes without a reliance on resolving an interface. Data mappers provide an easy way to ensure efficient information transfer between connected meshes as the introduced interpolation error tends to be very low.

The various studies performed to lend robustness to the method provide additional conclusions. For a steady-state model, CHT continua solvers looping frequency is not a critical factor to the simulation. The results between the four operating conditions tested (Op 1 - 4) demonstrated that this simulation parameter yields minor differences in temperature and incoming radiation values. Further analysis needs to be performed to optimize this parameter for convergence speed, along with further model development to study the impact of the frequency for specific continua. In comparing the Realizable 2-Layer $k-\epsilon$ all y+ and the SST $k-\omega$ models, it can be determined that both models provide good resolution of the thermal boundary layers and yield good results with the former trending closer to test data. Furthermore, the Realizable 2-Layer $k-\epsilon$ all y+ is seen as the more favorable choice as it is also understood to typically be more stable for different flow conditions. In comparing the polyhedral and trimmed cell meshes, it can be concluded that the polyhedral proved to be more effective for this simulation. The polyhedral mesher substantially outperformed the trimmed cell hexahedral mesher in solver time while providing very similar converged temperature values. It can be concluded that Radiation patch-face proportion is a critical factor in radiation resolution. It has been observed that the patch-face proportion resolution of primarily radiation source acting components has a small impact on the simulation, whereas the patch-face proportion on the sinks influence the results more. Further analysis is required to understand recommended values for patch-face proportion.

6
Future Work

It is essential to further explore the surface wrapper tool in order to maximize the advantage of its robustness and powerful features, which will result in obtaining a perfect surface wrapper which in turn is useful to obtain more accurate contacts and interfaces. Further exploration of interfaces method on large scale models is necessary to compare it with data mapper model of similar scale which was built in the course of this project.

Additionally, the future work can include eliminating the model simplifications made due to time restrictions. This would entail modeling more or the entirety of the truck under-hood and body within a solid continua, utilizing accurate material models. Internal flow structures modeled as boundary conditions, such as the internal powertrain gas flow, could also be simulated. This would lead to very heavy models impractical for common industrial use, but may provide useful insight as large scale simulation model validation.

Using the platform of steady state simulation model, transient models can be developed. Two transient simulations have been identified as notable items to evaluate the performance of the methodology. The first is a thermal soak simulation, simulating a hot engine into a key-off and subsequent thermal soak without forced convection into the under-hood region. The second transient simulation would include the development of pseudo-transient simulation model to evaluate the effects of differing road conditions such as rapid elevation changes.

Lastly, the further studies of the parameters explored in this work, particularly looping frequency and radiation patch-face proportion can be performed to identify optimal values for such a simulation methodology.

Bibliography

1. *Fact sheet: trucks — acea.auto* [Accessed 30-05-2024]. 2023. https://www.acea.auto/fact/fact-sheet-trucks/.
2. Council of European Union. *REGULATION OF THE EUROPEAN PARLIAMENT AND OF THE COUNCIL on type-approval of motor vehicles and engines and of systems, components and separate technical units intended for such vehicles, with respect to their emissions and battery durability (Euro 7) and repealing Regulations (EC) No 715/2007 and (EC) No 595/2009* 2022.
3. Council of European Union. *REGULATION OF THE EUROPEAN PARLIAMENT AND OF THE COUNCIL AMENDING REGULATION (EU) 2019/1242 AS REGARDS STRENGTHENING THE CO2 EMISSION PERFORMANCE STANDARDS FOR NEW HEAVY-DUTY VEHICLES AND INTEGRATING REPORTING OBLIGATIONS, AMENDING REGULATION (EU) 2018/858 AND REPEALING REGULATION (EU) 2018/956* 2024.
4. Council of European Union. *REGULATION (EU) No 540/2014 OF THE EUROPEAN PARLIAMENT AND OF THE COUNCIL of 16 April 2014 on the sound level of motor vehicles and of replacement silencing systems, and amending Directive 2007/46/EC and repealing Directive 70/157/EEC* 2019.
5. El-Sharkawy, A. E., Kamrad, J. C., Lounsberry, T. H., Baker, G. L. & Rahman, S. S. Evaluation of impact of active grille shutter on vehicle thermal management. *SAE International Journal of Materials and Manufacturing* **4,** 1244–1254 (2011).
6. Lidar, J. *Thermal Analysis of Engine Bay in Star-CCM+. Method Development and Correlation with Experimental Data.* MA thesis (Chalmers University of Technology, 2018). https://api.semanticscholar.org/CorpusID:125701874.
7. Svantesson, E. MA thesis (KTH, Mekanik, 2019).
8. Shim, H. R. & Park, J. M. *A Study of the Transient Analysis Technique on the Under Hood Thermal Damage* tech. rep. (SAE Technical Paper, 2011).
9. Wang, G., Gao, Q., Zhang, T. & Wang, Y. A simulation approach of underhood thermal management. *Advances in Engineering Software* **100,** 43–52 (2016).
10. Gu, W. & Su, W. Study on the Effects of Exhaust Gas Recirculation and Fuel Injection Strategy on Transient Process Performance of Diesel Engines. *Sustainability* **15.** ISSN: 2071-1050. https://www.mdpi.com/2071-1050/15/16/12403 (2023).
11. Lemort, V., Olivier, G. & de Pelsemaeker, G. in *Thermal Energy Management in Vehicles* 54–128 (John Wiley I& Sons, Ltd, 2023). ISBN: 9781119251767.

eprint: https://onlinelibrary.wiley.com/doi/pdf/10.1002/9781119251767.ch2. https://onlinelibrary.wiley.com/doi/abs/10.1002/9781119251767.ch2.

12. Versteeg, H. K. & Malalasekera, W. *An introduction to computational fluid dynamics - the finite volume method.* I–X, 1–257. ISBN: 978-0-582-21884-0 (Addison-Wesley-Longman, 1995).
13. Davidson, L. *Fluid mechanics, turbulent flow and turbulence modeling* https://www.tfd.chalmers.se/~lada/postscript_files/solids-and-fluids_turbulent-flow_turbulence-modelling.pdf (Chalmers University of Technology, 2024).
14. Rodi, W. *Experience with two-layer models combining the k-epsilon model with a one-equation model near the wall* in *29th Aerospace sciences meeting* (1991), 216.
15. Shih, T.-H., Liou, W. W., Shabbir, A., Yang, Z. & Zhu, J. A new k-epsilon eddy viscosity model for high reynolds number turbulent flows. *Computers & fluids* **24,** 227–238 (1995).
16. Menter, F. R. Two-equation eddy-viscosity turbulence models for engineering applications. *AIAA journal* **32,** 1598–1605 (1994).
17. Siemens Digital Industries Software. *Simcenter STAR-CCM+ User Guide v. 19.02* version 2402, 19.02. Siemens 2024.
18. Incropera, F. P., Bergman, T. L., Lavine, A. S. & DeWitt, D. P. *Incropera's Principles of Heat and Mass Transfer* (Wiley, 2017).
19. Yin, Z. & Fang, X.-j. *Investigation of film cooled turbine with conjugate heat transfer using source term model* in *Turbo Expo: Power for Land, Sea, and Air* **55157** (2013), V03BT13A016.

DEPARTMENT OF SOME SUBJECT OR TECHNOLOGY
CHALMERS UNIVERSITY OF TECHNOLOGY
Gothenburg, Sweden
www.chalmers.se

CHALMERS
UNIVERSITY OF TECHNOLOGY